Polymer Reviews, 50:474–510, 2010

ISSN: 1558-3724 print / 1558-3716 online
DOI: 10.1080/15583724.2010.515764

Taylor & Francis
Taylor & Francis Group

A Review on the Development of the Inverted Polymer Solar Cell Architecture

STEVEN K. HAU, HIN-LAP YIP, AND ALEX K.-Y. JEN

Department of Materials Science and Engineering, University of Washington, Seattle, WA 98195-2120, USA

The increase in energy production costs for fossil fuels has led to a search for an economically viable alternative energy source. One alternative energy source of particular interest is solar energy. A promising alternative to inorganic materials is organic semiconductor polymer solar cells due to their advantages of being cheaper, light weight, flexible and made into large areas by roll-to-roll processing. However, the conventional architecture that is typically used for fabricating solar cells requires high vacuum to deposit the top metal electrode which is not suitable for roll-to-roll processing. Recently an inverted device architecture has been investigated as a suitable architecture for developing the ideal roll-to-roll type processing of polymer-based solar cells. This review will go over the recent advances and approaches in the development of this type of inverted device architecture. We will highlight some of the work that we have done to integrate materials, device, interface, and processing of the inverted device architecture platform to produce more idealized polymer-based solar cells.

Keywords inverted device architecture, polymer solar cell, interface engineering, self assembled monolayers

1. Introduction

Recently, organic polymer photovoltaic cells have attracted a significant amount of attention due to the need to develop an inexpensive clean and sustainable renewable energy source. Polymer-based photovoltaic cells have the advantage of being less expensive and solution-processible by roll-to-roll type processing techniques.[1] The most widely studied polymer blend system is based on a solution processed p-type poly(3-hexyl-thiophene) (P3HT) polymer and an n-type [6,6]-phenyl C_{61} butyric acid methyl ester (PCBM) fullerene. This polymer blend system has led to efficiencies as high as 5%.[2,3] Efficiencies as high as 6 to 7% have been achieved with polymer:fullerene bulk-heterojunction (BHJ) systems by developing lower band-gap polymer materials that can absorb a broader range of the solar spectrum.[4–6] The BHJ device configuration is achieved by blending the n-type and p-type materials to increase the number of interfaces between the donor and acceptor phases in order to provide more exciton dissociation/charge separation sites to generate more charge carriers. Generally, phase segregation of the blend materials greater than ~10–20 nm will lead to lower photocurrents from the high charge recombination rates due to the low mobility of the conjugated materials.

Received April 17, 2010; accepted August 9, 2010.
Address correspondence to Alex Jen, Dept of Materials Science and Engineering, Box 352120, University of Washington, Seattle, WA 98195. E-mail: ajen@u.washington.edu

The BHJ concept has generally been implemented into the conventional device architecture. This architecture consists of a transparent conducting metal oxide coated with a poly(3,4-ethylenedioxythiophene):poly(styrenesulfonate) (PEDOT:PSS) hole-transporting layer followed by the active BHJ layer. To complete the device, a low work function metal electrode (Al, Ca/Al) is evaporated on top as an electron-collecting electrode. Although the majority of polymer-based solar cells are fabricated in the conventional architecture, there are concerns with the inherent device stability. The transparent conducting indium tin oxide (ITO) used as the hole collecting contact can be etched over time upon exposure to the acidic PEDOT:PSS hole-transporting buffer layer.[7,8] Replacing the PEDOT:PSS layer with other hole-transporting layers have so far been unsuccessful in maintaining high conversion efficiencies due to the high resistance of the transporting layer.[9] The low work function electrode used in this device architecture requires high vacuum deposition leading to increases in fabrication costs. Additionally, ambient exposure can lead to oxidation of these electrodes leading to device degradation and failure.[10] Electron selective buffer layers (TiO_2, ZnO) have been successfully inserted between the top metal electrode and organic active layer to minimize oxygen diffusion leading to improved device stability.[11–13] However, this still requires high vacuum deposition of the metal electrodes to complete the device.

Device architectures that remove PEDOT:PSS at the ITO interface and use non-vacuum deposited high work function metal electrodes at the top interface are needed. Based on these considerations, an inverted device architecture where the nature of the charge collection is reversed was proposed as a good device alternative. This architecture has recently gained considerable research attention due to the device stability and processing advantages compared to the conventional architecture. In this inverted architecture, the polarity of charge collection is the opposite of the conventional architecture allowing the use of higher work function (Au, Ag, Cu) and less air-sensitive electrodes as the top electrode for hole collection. The use of higher work function metals offer better ambient interface device stability and the possibility for using non-vacuum coating techniques to deposit the top electrode helping to reduce fabrication complexity and costs.[14–16] Most of the research attention for these inverted device architectures has been to understand how to improve the device efficiency, stability, and processing of the different interface layers in the device structure. The inverted architecture can be differentiated by the direction of the incoming light source illuminating the solar cells (top illuminated or bottom illuminated solar cell architecture). The top illuminated architecture utilizes a reflective buried bottom electrode and a semi-transparent top electrode whereas the bottom illuminated inverted architecture configuration utilizes a higher work function reflective electrode as the top hole collecting contact and a semi-transparent conducting electrode at the bottom to collect electrons. These two types of inverted solar cells architectures have been successfully demonstrated in literature, but most research has been focused on the bottom illuminated type inverted solar cell. This is due to the difficulty in finding a suitable transparent conducting top electrode material for top illuminated devices.

In the top illuminated inverted solar cell configuration, the requirements are that the top electrode needs to be semi-transparent so that light can reach the active layer. This type of architecture was demonstrated by Glatthaar et al. In this architecture, a thin film of aluminum was deposited onto glass followed by a titanium film. An active layer of polymer was deposited on top followed by a PEDOT:PSS/Au grid layer.[17] Efficiencies of 1.4% were demonstrated using the PEDOT:PSS/Au grid semi-transparent top electrode configuration. Chen et al. also demonstrated a top illuminated type inverted device with efficiency of 3%.[18] The difference in this device configuration was that a flexible stainless

steel metal foil was used as the substrate instead of a glass substrate. The sequence of layers deposited on top of the stainless steel foil were Ag, ITO, Cs_2CO_3, P3HT:PCBM active layer, MoO_3, Al metal grid and ITO. Since these devices were fabricated onto flexible foils, a flexural test was performed showing good mechanical stability with only a 12% decrease in efficiency after 450 bending cycles. The top illuminated inverted configuration was also demonstrated onto a polymer flexible substrate. Instead of a metal foil, a surface-nickelized polyimide film was used. A thin layer of titanium oxide precursor was cast onto the surface-nickelized polyimide film, followed by a P3HT:PCBM active layer, and a high conductivity PEDOT:PSS top electrode showing efficiency of up to 2.4%.[19]

In the bottom illuminated inverted solar cell configuration, a high work function electrode is utilized at the top to collect holes and an interface layer is used to modify the ITO interface to effectively collect electrons. Some of the interface layers that have been utilized to modify the ITO for effective electron collection are Cs_2CO_3,[20,21] Ca,[22] ZnO,[10,23,24] and TiO_2.[25–27] Since light needs to pass through these layers to reach the active layer to generate a photocurrent, the layers are typically very thin for maintaining high transparency. Direct contact of the top high work function metal to the active layer can lead to degradation of the solar cell performance; therefore, hole transporting/electron blocking layers have been also deposited between these layers to improve charge selectivity and collection of holes. Some materials that have utilized at the active layer and metal interface are based on various transition metal oxides (MoO_3,[28–30] WO_3,[31,32] V_2O_5,[33–35]) and solution processed conducting polymers (PEDOT:PSS,[10,24–26] SPDPA[36]).

Combining cesium carbonate (Cs_2CO_3) and vanadium oxide (V_2O_5), Li et al. demonstrated that by placing these two interface layers at different locations in the device layer stack, the polarity of the solar cell can be changed from a conventional device to an inverted device architecture.[20] An inverted solar cell device was demonstrated by evaporating a thin Cs_2CO_3 (~1 nm) at the ITO interface and a thin V_2O_5 (~10 nm) layer between the active P3HT:PCBM layer and top metal electrode leading to an efficiency of 2.25%. Replacing the evaporated Cs_2CO_3 with a solution processed Cs_2CO_3 layer showed very similar conversion efficiency ~2.1%. In another study by the same group, efficiency as high as 4.2% in inverted solar cells was achieved using the solution processed Cs_2CO_3 based interface layer system.[21] Upon annealing the Cs_2CO_3 at 150°C, the Cs_2CO_3 was found to decompose to doped cesium oxide (Cs_2O) helping to reduce the work function from -3.45 eV to -3.06 eV favoring improved electron collection.

N-type metal oxides (ZnO and TiO_2) are more commonly utilized as the interface modification layer at the ITO interface for inverted solar cells due to the high optical transparency in the visible and near infrared, high carrier mobility, and its solution processibility. The energy levels of these metal oxides (LUMO and HOMO) have been reported to be around −4.4 eV and −7.6 eV, respectively. The low LUMO and high HOMO levels allow these materials to be a good electron selective layer and hole-blocking layers. Many demonstrations of using these n-type metal oxide layers as the electron selective layer for inverted solar cells have been reported in literature. An efficient inverted solar cell from a high temperature processed sol-gel ZnO underlayer on ITO and an Ag electrode as the top hole collecting contact was demonstrated by White et al.[23] The ZnO sol-gel was thermally annealed at 300°C for 5 min to crystallize the ZnO to improve its conductivity and mobility leading to conversion efficiencies of 2.97%. When these devices were exposed to air, it was found that the device performance improved. They attribute the improvement to the oxidation of Ag which caused a shift in the effective work function closer to the HOMO of P3HT leading to improved ohmic contact. It was found that devices stored in nitrogen with periodic exposure to air maintained a device efficiency of 2.32% even after

7 days of storage. A thin titanium oxide sol-gel layer (~10 nm) at the ITO interface was also demonstrated as an effective electron selective layer for use in inverted solar cells.[25] Devices were fabricated from a solution of P3HT:PCBM in o-xylene with a solution processed PEDOT:PSS interface layer between the active layer and Au top electrode showing efficiencies of 3.1%. The authors found using o-xylene as a solvent segregates more PCBM at the bottom (electron collection interface) which is better for inverted solar cells. Controlling the bulk blend vertical phase segregation of one of the materials towards a particular charge collecting interface is important to minimize losses in photocurrent and efficiency caused from charge recombination due to poorly distributed phases. The vertical phase segregation of the donor and acceptor blend materials in the bulk-heterojunction has already been shown by many research groups to have a dramatic effect on the performance of polymer-based solar cells.[37–41] In another study by the same group, a thin polyoxyethylene tridecylether (PTE) (~10 nm) was coated on the ITO surface prior to coating a thin titanium oxide layer in an inverted solar cell leading efficiencies of ~3.6%.[26] It is suggested that the improvement in the efficiency is that the passive PTE layer improves the surface quality for better titanium oxide wetting of the surface, therefore providing a more intimate interface with the active layer.

In addition to modifying the ITO surface with interface layers for inverted solar cells, transition metal oxides (MoO_3, WO_3, and V_2O_5) have also been used to modify the interface between the active layer and top metal electrode. These metal oxide layers are usually deposited by means of vacuum deposition. Inverted solar cell with 2.57% efficiency have been demonstrated using vacuum deposited MoO_3/Ag as the top metal contact and high temperature annealed TiO_2 at the ITO interface.[29] Further improvement in efficiency to 3.09% was demonstrated using high temperature annealed ZnO at the ITO interface and vacuum deposited MoO_3/Ag at the top electrode.[28] Efficiency of 3.55% was achieved using a MoO_3 as the top buffer layer and Ca as the electron collecting layer at the ITO interface in inverted solar cells.[22] Semi-transparent inverted devices were demonstrated using MoO_3/sputtered ITO as the top electrode and atomic layer deposited titanium dioxide at the bottom ITO interface to collect electrons. The MoO_3 buffer layer prevented damage to the active layer from the sputtering process of the ITO coating leading to 1.9% efficiencies.[30] WO_3 and high temperature processed TiO_2 inverted solar cells have also been demonstrated with 2.58% efficiencies.[31] Inverted cells using a solution processed V_2O_5 and evaporated Ag metal contact on top with ZnO at the ITO interface have also been demonstrated showing efficiencies of 3.56%.[33] The use of a solution processible method to cast the buffer layer on top has the advantage of minimizing the fabrication complexity which can lead to lowering of fabrication costs. Other solution processible materials that have been utilized as buffer layers between the active layer and top metal electrode have been based on solution processible polymers such as PEDOT:PSS and self-doped sulfonated poly(diphenylamine) (SPDPA). Li et al. demonstrated inverted solar cell efficiencies of 3.91% using SPDPA as the hole collecting buffer layer between the active layer and the top metal electrode.[36]

The ideal fabrication process for polymer-based solar cells would be to utilize solution processing techniques to deposit the different layers onto flexible substrates so that it allows for the potential to be used for simple roll-to-roll type processing. Additionally, the solar cells should maintain high device stability and efficiency over a certain period of time. The inverted device architecture has the potential to combine all of these requirements—device flexibility, stability, efficiency, and solution processibility into one system. However, in order to achieve this more ideal polymer-based solar cell system an integrated engineering approach to develop materials, devices and improve interfaces and processing are required. The following will review some of the work that we have done to integrate materials,

device, interface, and processing onto the inverted device architecture platform to produce a more idealized polymer-based solar cell.

2. Inverted Polymer-Based Solar Cells

2.1 Inverted Polymer-Based Solar Cells on Flexible Substrates

Many studies on the inverted device architecture have utilized n-type inorganic metal oxides (ZnO, TiO_2) as the electron selective layer between the active layer and the ITO semi-transparent electrode. However, most of the electron selective layers require high temperature annealing processing conditions in order to improve the crystallinity of the material to minimize resistive losses in the solar cell devices. These high temperature processing conditions can reach as high as 500°C which is not compatible with the processing of solar cells on flexible polymer substrates. The use of flexible plastic based substrates requires that the electron selective layer to be processed at low temperatures in order to minimize degradation to the substrate. From this consideration, a method to fabricate and process a room temperature electron selective layer of n-type ZnO nanoparticles (ZnO-NPs) was demonstrated on a flexible inverted polymer solar cell. The feasibility of replacing high temperature processed sol-gel layers of ZnO with a room temperature processed ZnO-NPs layer was studied by X-ray diffraction of the ZnO layers and by fabrication of inverted solar cell devices. Devices on glass/ITO substrates using the high temperature ZnO sol-gel are compared to those fabricated using the ZnO-NPs layer.

X-ray diffraction studies were performed on room temperature processed films of the ZnO NPs and the sol-gel processed ZnO after thermal annealing at 400°C (Fig. 1). Both the thermal annealed ZnO and ZnO NPs show three typical crystalline ZnO peaks at 31.8° (100), 34.3° (002), and 36.3° (101) indicating that both films have crystallinity regions. Devices were fabricated using these processing conditions for the two electron selective layers. Table 1 shows the average device performance of the inverted solar cells fabricated

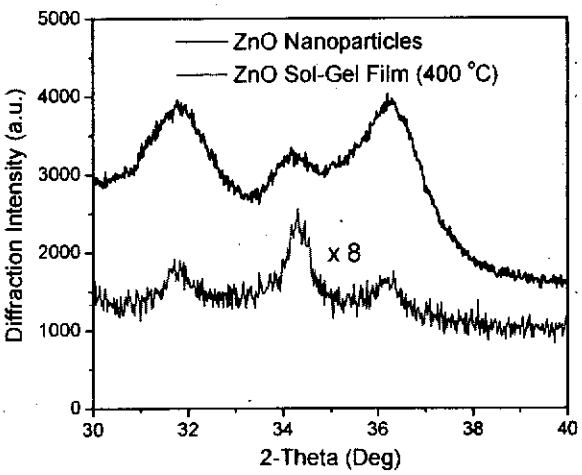

Figure 1. X-ray diffraction of ZnO NPs at room temperature and sol-gel processed ZnO after thermal annealing at 400 °C showing three distinct ZnO crystalline peaks at 31.8° (100), 34.3° (002), and 36.3° (101). Adapted with permission from.[10] Copyright 2008 American Institute of Physics. (Figure available in color online)

Table 1
Average device performance of un-encapsulated inverted P3HT:PCBM bulk heterojunction solar cells using sol-gel processed or ZnO NPs on ITO/glass and ZnO NPs on ITO/plastic. Adapted with permission from.[10] Copyright 2008 American Institute of Physics

Substrate Electrode	ZnO	Voc (V)	Jsc (mA/Cm^2)	FF (%)	PCE (%)
Glass/ITO Ag	ZnO Sol-Gel	0.62	11.1	51.3	3.5
Glass/ITO Ag	ZnO-NPs	0.62	10.7	54.2	3.6
Plastic/ITO Ag	ZnO-NPs	0.62	9.8	53.9	3.3

onto ITO/glass substrates on the ZnO sol-gel and ZnO-NPs electron selective layer as well as devices fabricated from the ZnO-NPs onto flexible plastic substrates. The active layer used in these studies is based on a bulk-heterojunction blends of P3HT:PCBM at a weight ratio of 1:0.6 and thermally annealed at 160°C. The devices fabricated from the ZnO-NPs on ITO-coated glass show an average PCE of ~3.6%. This value is very similar to that obtained from the high temperature processed ZnO sol-gel devices on glass/ITO which show an average efficiency of ~3.5%. This demonstrates that both the sol-gel ZnO and ZnO-NPs derived layers both behave similarly as a good electron selective layer in the inverted device architecture. To demonstrate that the ZnO-NPs layer can be used onto flexible plastic substrates, inverted devices were fabricated onto ITO-coated plastic substrates showing an average PCE of ~3.3%. However, a slightly lower efficiency is observed with these devices which is attributed to the lower transparency (~80%) of the ITO-coated plastic in the region of 500–600 nm compared to ITO-coated glass (~88%) which reduces the photon flux to the active layer as indicated from the lower J_{sc}. Nonetheless, the use of a low temperature process electron selective layer with high efficiency onto flexible plastic substrates was demonstrated which is important for the development of roll-to-roll type processing.

2.2 Stability of Inverted Polymer-Based Solar Cells

2.2.1 Air-Stablity of Inverted Polymer-Based Solar Cells. The architecture of the inverted device allows for the use of a more air-stable higher work function top electrode to collect holes such as Ag or Au. Because of the higher work function electrode utilized at the top, the device stability should to be improved. White et al. found that using an Ag electrode in the inverted device architecture did maintain improved stability under nitrogen atmosphere.[23] However, unencapsulated inverted solar cells under ambient air exposure conditions have not been studied. To study the effect of the devices under ambient air exposure, unencapsulated inverted solar cells and conventional solar cells were fabricated and periodically tested and stored in air for 40 days (Fig. 2). The conventional device using LiF/Al as the electrode was extremely unstable as its PCE was reduced to less than half of its original value after 1 day of storage and totally degraded after 4 days. The FF and V_{oc} decrease dramatically after 1 day of air exposure due to the interface instability of the electrode from oxidation of the aluminum. The *J-V* characteristics of the conventional device as a function of storage time in ambient are plotted in Fig. 3(a). The plots show a dramatic decrease in photocurrent in the first couple of days and show negligible photocurrent after 4 days of air exposure. The inset of Fig. 3(a) illustrates the dark current diode characteristics for which the device exposed to 4 days in ambient has a two orders of decrease in the current density at 2V compared to its initial state. The

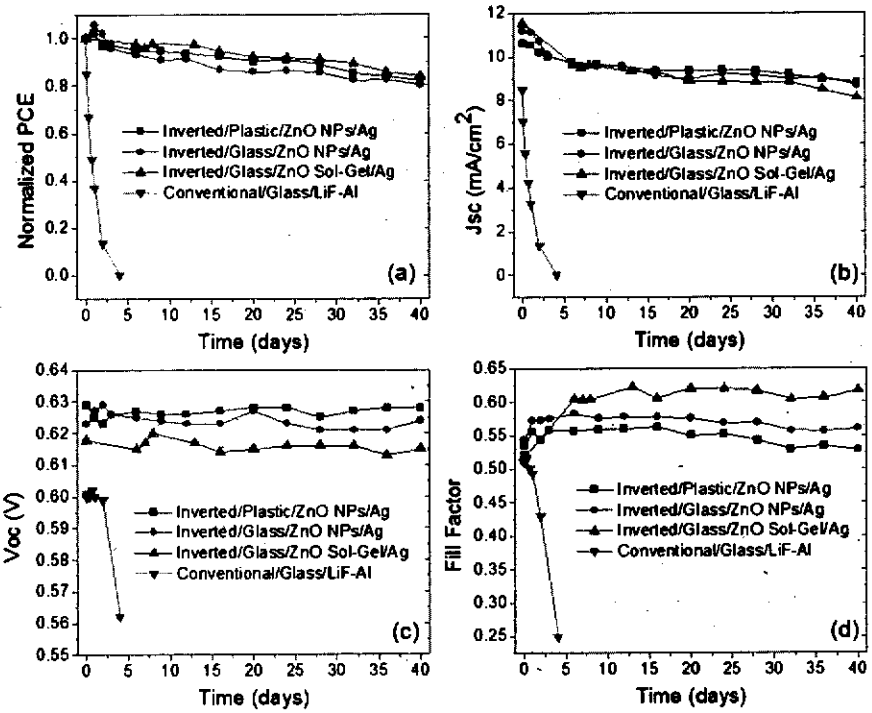

Figure 2. Device performance of un-encapsulated conventional and inverted solar cells stored 40 days in air under ambient conditions. (a) Normalized power conversion efficiency (PCE), (b) Short-circuit current density (J_{sc}), (c) Open-circuit voltage (V_{oc}), (d) Fill factor. Adapted with permission from.[10] Copyright 2008 American Institute of Physics. (Figure available in color online)

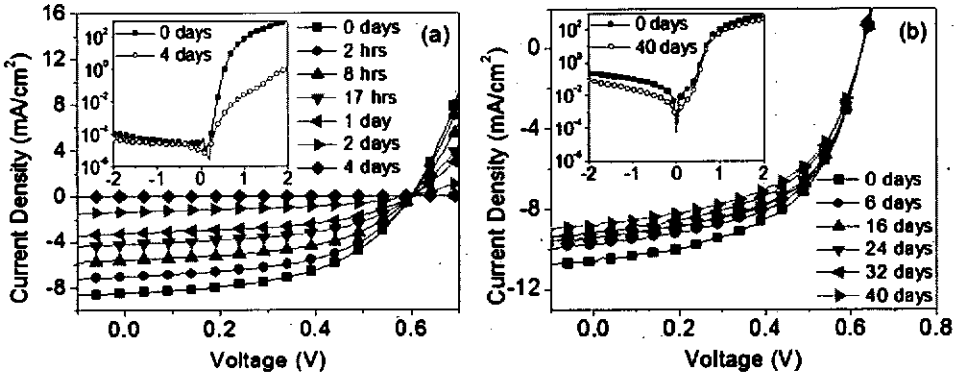

Figure 3. (a) *J-V* characteristics of un-encapsulated conventional P3HT:PCBM bulk-heterojunction solar cells over a period of 4 days in air under ambient conditions. (b) *J-V* characteristics of un-encapsulated inverted P3HT:PCBM bulk-heterojunction solar cells (ZnO NPs on ITO-coated plastic substrate) over a period of 40 days in air under ambient conditions. Inset: un-encapsulated dark current device characteristics at 0 days and 40 days in air under ambient conditions. Adapted with permission from.[10] Copyright 2008 American Institute of Physics. (Figure available in color online)

inverted devices however, showed high stability to ambient exposure showing constant FF and V_{oc} values over the period of 40 days while the J_{sc} slightly decreased over this time leading to normalized PCE of over 80%. Figure 3(b) shows a typical flexible inverted unencapsulated device exposed to ambient. The improved in-device stability is attributed to both the PEDOT:PSS layer and Ag electrode. The PEDOT:PSS can effectively prolong oxygen diffusion to the active layer. Additionally, the Ag electrode in air can form a layer of silver oxide thereby increasing its effective work function to −5.0 eV. This matches well with the PEDOT:PSS HOMO of −5.1 eV which improves its electrical coherence at the interface.[23,42,43] By having devices stable in air, the encapsulation process can be performed under ambient conditions substantially reducing fabrication complexity leading to cost-effective solar cells.

2.2.2 Thermal Stability of Inverted Polymer-Based Solar Cells. In addition to the ambient device stability, another concern with polymer-based solar cells is the morphological stability of the BHJ blend phases. The phase-separated morphology of the blends are not very thermodynamically stable due the fact that the materials still have a certain degree of freedom to diffuse slowly or recrystallize over time. This is especially true under elevated temperatures which can lead to gradual changes in the nanostructure and microstructure.[44,45] The two components will segregate into larger phases leading to reduction in the number of interfaces causing degradation in the device performance. There have been several strategies that have been developed to improve the thermal and morphological stability of P3HT:PCBM BHJ active layers. One is to change the polythiophene backbone to induce a controlled amount of disorder which helps to suppress the crystallization-driven phase segregation between the polymer and fullerene.[46,47] Another method is to utilize diblock copolymers additives in the BHJ film to help stabilize the film from phase segregation.[48] Another method found to be an effective one to stabilize the nanophase segregration is to utilize similar chemical motifs in both the polymer and fullerene used in the blend system.[49] In our approach, amorphous fullerene derivatives are synthesized and utilized as the electron accepting material in P3HT:fullerene based BHJ inverted solar cells.[50] The amorphous fullerenes studied are based on modifications to PCBM by replacing the planar phenylene ring with a bulky triphenylamine (TPA) or 9,9-dimethylfluorene (MF). The aim was to suppress the crystallization induced morphological changes that cause device degradation.

2.2.2.1 Electrochemical, Thermal, and Electrical Properties of TPA-PCBM and MF-PCBM Derivatives. The electrochemical properties of the amorphous fullerene derivatives were studied by cyclic voltammetry as shown in Fig. 4. The fullerenes all show four quasi-reversible one-electron reduction waves, which are attributed to the fullerene core. The first reduction potential (E_1^{red}) corresponding to the LUMO level of PCBM is shifted to a more negative value as compared to the parent C_{60} (Fig. 4) due to the release of strain energy after the introduction of the [6,6] methane substitute on C_{60}.[51–53] The stronger electron-donating properties of the TPA and MF compared to benzene results in a reduction wave shift toward more negative potentials. Differential scanning calorimetry (DSC) of PCBM, TPA-PCBM, and MF-PCBM are shown in Fig. 5. The results show that PCBM has a crystallization peak at 295°C with no additional transitions between 20 and 350°C. Both the TPA-PCBM and MF-PCBM show a glass transition (T_g) of 170°C and 180°C, respectively.

One of the more important properties that can drastically influence the performance of polymer-based BHJ solar cell is the mobility of the materials. The electron mobilities of TPA-PCBM and MF-PCBM are compared to PCBM in an n-channel organic field effect transistor (OFET) device configuration. All of the PCBMs showed typical n-type OFET behavior with saturation field-effect electron mobilities of 1.6×10^{-2}, 1.1×10^{-2}, $5.4 \times$

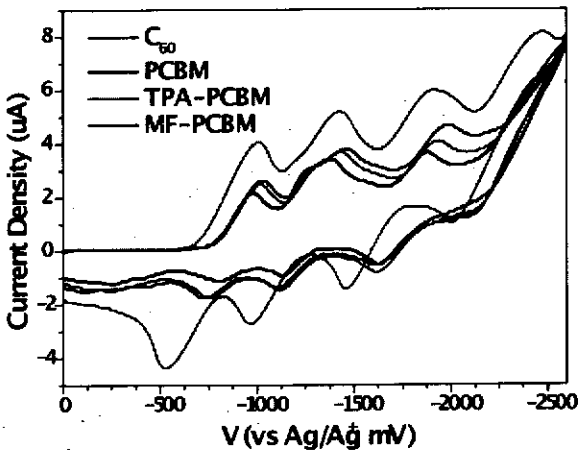

Figure 4. Cyclic voltammograms of C_{60}, PCBM, TPA-PCBM and MF-PCBM in 1,2-dichlorobenzene solution. Adapted with permission from.[50] Copyright 2009 American Chemical Society. (Figure available in color online)

10^{-3} $cm^2/V \cdot s$ for PCBM, TPA-PCBM, and MF-PCBM respectively. The slight decrease in the mobilities of the two amorphous fullerenes compared to PCBM is attributed to the bulky substituent from the triphenylamine and dimethylfluorene.

2.2.2.2 Device Characteristics of Inverted Polymer-Based Solar Cells with Amorphous Fullerenes. These amorphous fullerenes are compared to PCBM as the electron accepting material in the active layer of inverted devices and the *J-V* characteristics of these devices are shown in Fig. 6. The conversion efficiencies of the TPA-PCBM and MF-PCBM devices were 4.0% and 3.8%, respectively, which is comparable to those fabricated with PCBM as the n-type material (4.2%). The open-circuit voltage (V_{oc}) of the TPA-PCBM and MF-PCBM was 0.65 V, whereas the PCBM devices only had a V_{oc} of 0.63 V. The 20 mV increase in V_{oc} compared to PCBM is in agreement with what is observed in the shift in LUMO

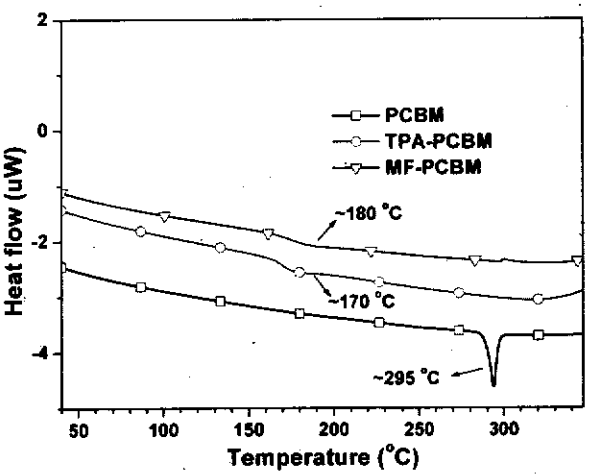

Figure 5. DSC curves of PCBM, TPA-PCBM and MF-PCBM. Adapted with permission from.[50] Copyright 2009 American Chemical Society. (Figure available in color online)

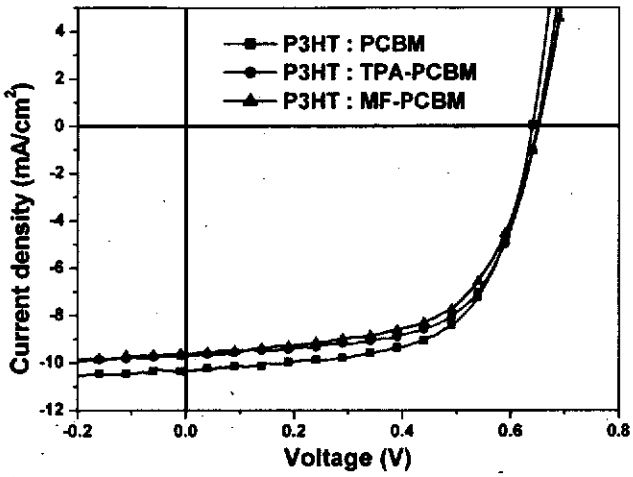

Figure 6. The J-V curves of PCBM, TPA-PCBM and MF-PCBM-based BHJ devices under AM1.5 illumination at 100 mW/cm^2. Adapted with permission from.[50] Copyright 2009 American Chemical Society. (Figure available in color online)

level as seen by cyclic voltammetry. The slight differences in short circuit current density (9.9 mA/cm^2 for TPA-PCBM and 9.8 mA/cm^2 for MF-PCBM) as compared to PCBM (10.4 mA/cm^2) are attributed to the lower mobility of the two amorphous fullerenes.

The thermal stability of these solar cells is examined by annealing the BHJ films at a typical post-treatment temperature of 150°C for a time period of 10 min to 10 hours. Figure 7 shows the dependence of the PCE on the annealing time of the three different systems. In the system with PCBM as the acceptor, a gradual degradation in the device performance is observed with prolonged annealing time. The PCE of the PCBM system was 4.2% after 10 min of annealing and gradually decreased to 1.8% after annealing for

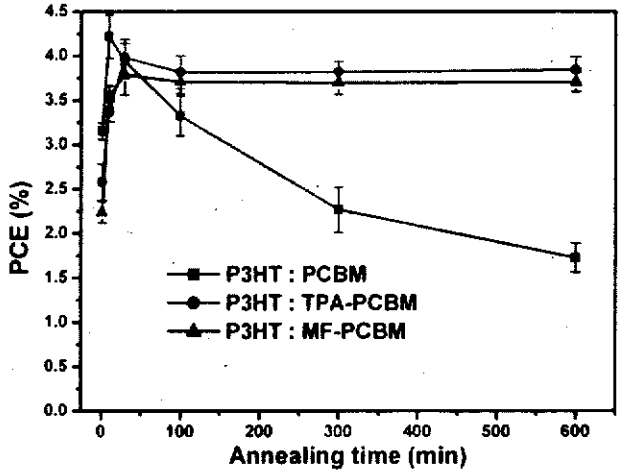

Figure 7. Plot of PCE vs annealing time of PCBM, TPA-PCBM and MF-PCBM-based devices annealed at 150°C. Adapted with permission from.[50] Copyright 2009 American Chemical Society. (Figure available in color online)

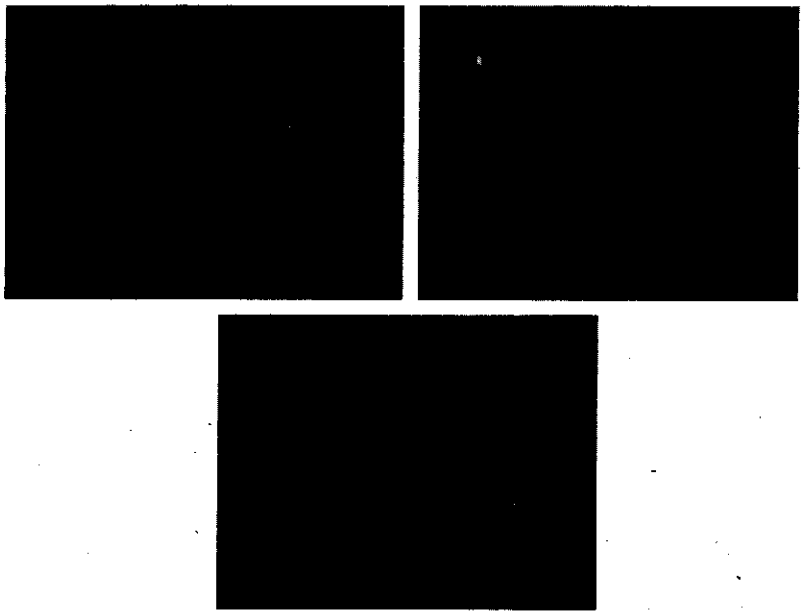

Figure 8. Optical images of (a) P3HT:PCBM, (b) P3HT:TPA-PCBM and (c) P3HT:MF-PCBM films after annealing at 150°C for 600 mins. Adapted with permission from.[50] Copyright 2009 American Chemical Society. (Figure available in color online)

10 hours. However, both the TPA-PCBM and MF-PCBM show a significantly higher thermal stability showing negligible PCE loss even after 10 hours of annealing. To understand the origin of the improved thermal stability, optical micrographs (Fig. 8) of the different fullerene active layer systems after annealing for 10 hours were taken. The optical image shows severe aggregation and microcrystallites in the P3HT:PCBM films annealed for 10 hours whereas both the TPA-PCBM and MF-PCBM films show no signs of severe phase segregation even after 10 hours of annealing. Atomic force microscopy (AFM) also show severe crystallization in the PCBM blend films whereas both the amorphous fullerene blend films have a surface roughness in the range of 1.3–1.5 nm rms (Fig. 9). These amorphous fullerene compounds show comparable electron mobilities to PCBM in OFETs and high power conversion efficiencies (~4%) in P3HT:fullerene polymer solar cells. The thermal stability of the polymer solar cells are remarkably enhanced and show no significant degradation in morphology or solar cell performance after annealing at 150°C for 10 hours whereas PCBM devices degraded dramatically. These amorphous based fullerene acceptors are attractive candidates for improving the long-term thermal and morphological stability of inverted based BHJ polymer solar cells.

2.3 Interface Modification of Inverted Polymer-Based Solar Cell with Self-Assembled Monolayers

Even though reasonable efficiencies have been reached with n-type metal oxides as the electron selective layer in inverted solar, it is known that the surface of metal oxides have hydroxyl groups that have been shown to cause charge trapping at the interface.[54] These hydroxyl terminated surfaces lead to high charge carrier recombination due to poor charge

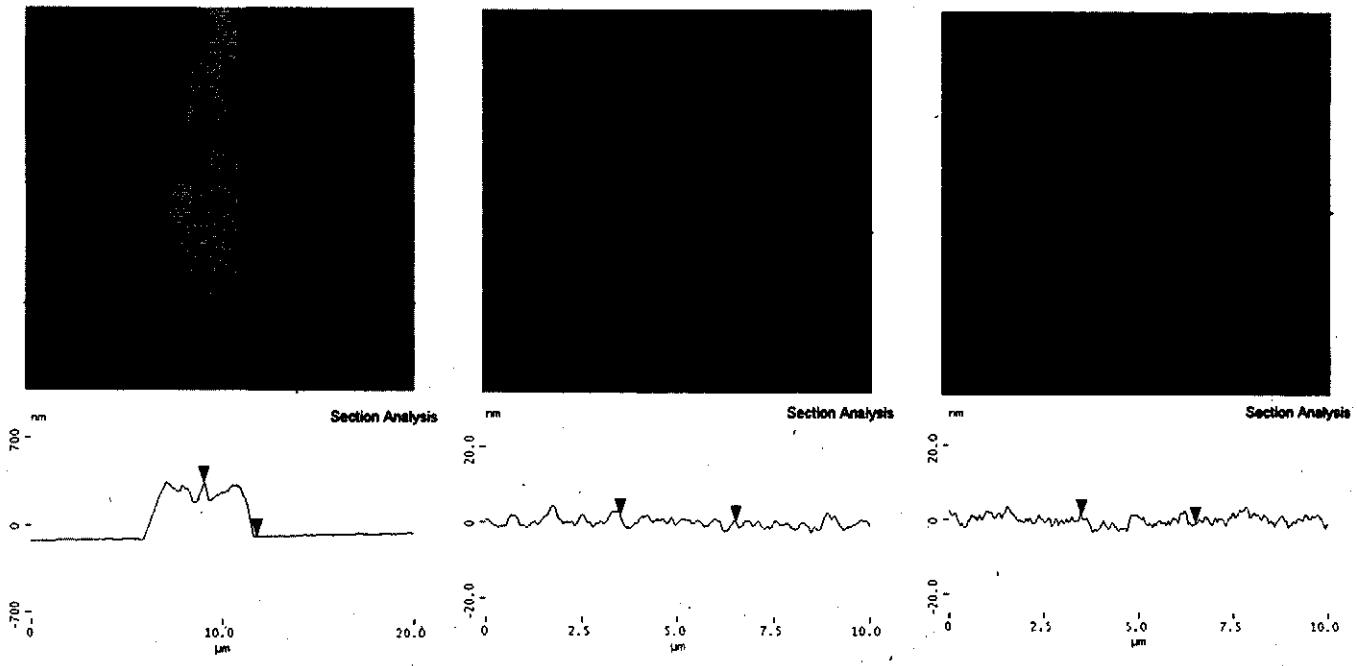

Figure 9. AFM images of (a) P3HT:PCBM, (b) P3HT:TPA-PCBM and (c) P3HT:MF-PCBM film annealed at 150°C for 600 min. Adapted with permission from.[50] Copyright 2009 American Chemical Society. (Figure available in color online)

transfer leading to losses in device performance. This increase in resistance across these interfaces needs to be minimized by appropriately controlling the electrical contacts (contact resistance, charge transfer, energy level alignment) to allow efficient collection of charges. Additionally, the poor morphological distribution of phases in the bulk-heterojunction active layer may also lead to high resistances in the solar cell due to high recombination of charge carriers. To improve the device parameters (PCE, J_{sc}, FF, and V_{oc}) and minimize resistance losses in the active layer, the size and distribution of phases needs to be appropriately controlled.

One approach that can both reduce the resistance across the metal oxide interface and affect the active layer morphology is to utilize a self-assembled monolayer (SAM) between the inorganic and organic interface. SAMs can be utilized to significantly modify the interfaces of oxide and metallic surfaces to improve adhesion, compatibility, charge transfer properties, energy level alignment, and affect the upper layer growth of materials.[13,24,27,55–58] We have demonstrated that modifying the metal oxide surfaces of TiO_2 and ZnO based inverted solar cells with a fullerene-based self-assembled monolayer (C_{60}-SAM) can improve the device performance. The C_{60}-SAM affects the photoinduced charge transfer at the interface to reduce the recombination of charges, passivate inorganic surface trap states, improve the exciton dissociation efficiency at the polymer/metal oxide interface as well as act as a template to influence the overlayer bulk-heterojunction distribution of phases and crystallinity leading to higher efficiency inverted solar cells.[24,27]

2.3.1 Inverted Solar Cells: Modification of TiO_2 Electron Selective Layers with Self-Assembled Monolayers.

2.3.1.1 Effect of the Self-Assembled Monolayers on Bulk-Heterojunction Solar Cells. The device structure of the TiO_2 based inverted polymer solar cells with the different types of surface modified SAMs are shown in (Fig. 10). The *J-V* characteristics for the inverted bulk-heterojunction cells modified with carboxylic acid SAMs are shown in Fig. 11. A summary of the average device performance modified with and without the monolayers is given in Table 2. The devices without SAM modification have an average power conversion efficiency (PCE) of 2.8% with a $J_{sc} = 9.8$ mA/cm^2, a $V_{oc} = 0.61$ V, and a FF = 46.9. When modified with the SAM, the devices show overall improvement in series resistance

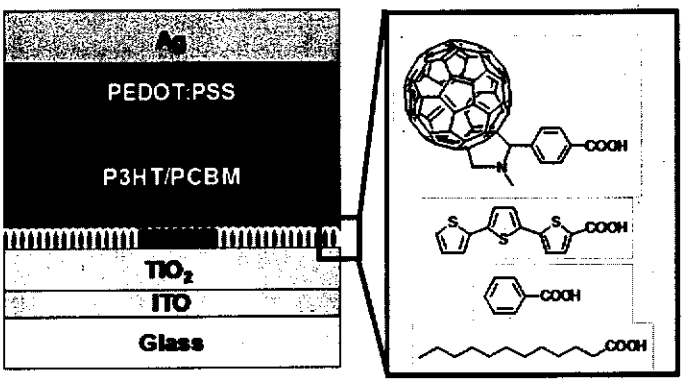

Figure 10. Device architecture of the inverted polymer solar cell with the different carboxylic acid based self-assembled molecules used to modify the TiO_2 surface. (Right side, top to bottom) C_{60} based SAM, terthiophene SAM, benzoic acid SAM, and lauric acid SAM.[27]—*Reproduced by permission of The Royal Society of Chemistry.* (Figure available in color online)

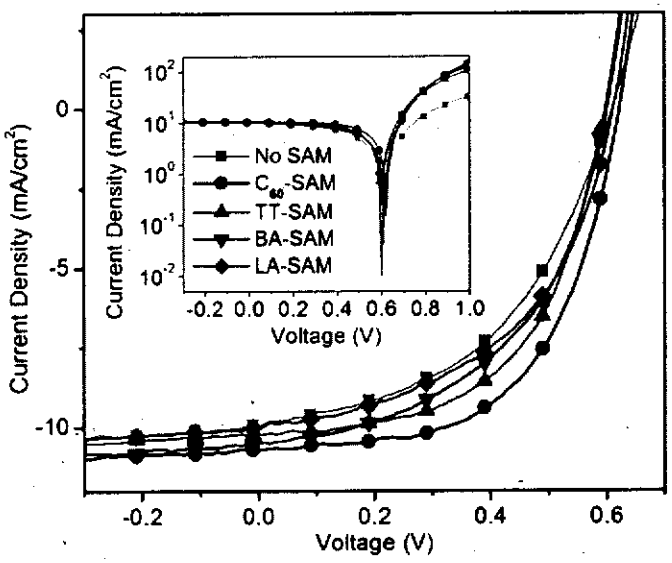

Figure 11. *J-V* characteristics of the inverted P3HT:PCBM bulk-heterojunction solar cells modified with and without self-assembled monolayers. (inset: plot of illuminated *J-V* curve in log scale).[27]—*Reproduced by permission of The Royal Society of Chemistry.* (Figure available in color online)

(R_s) from 13 $\Omega \cdot cm^2$ to 3–4 $\Omega \cdot cm^2$ and shunt resistance (R_{sh}) compared to devices without modification. The LA-SAM shows a slight improvement in PCE to 3.0%. The J_{sc} and V_{oc} remain similar to devices without a monolayer; however, the FF increases slightly to 49.5% which is attributed to the reduced surface traps leading to better contact. Modification with BA-SAM shows further improvement in PCE to 3.2%. The FF is similar to that of devices modified with LA-SAM; however, an increase in J_{sc} is observed. The J_{sc} improvement is attributed to BA-SAM improving the interface electron transfer by removing the trap states at the interface of the TiO_2 layer as described by Moser et al.[59] Modifying the surface with an electroactive functional group like terthiophene or C_{60} shows efficiency improvements of 0.6% and 1.0%, respectively when compared to devices without modification. A dramatic increase in FF of 56.2% and 57.2% in the TT-SAM and C_{60}-SAM, respectively is observed indicating that the electroactive groups on the SAM help to reduce the charge recombination

Table 2

Summary of the average device performance of inverted P3HT:PCBM bulk-heterojunction solar cells with and without carboxylic acid self-assembled monolayer modification.[27]—Reproduced by permission of The Royal Society of Chemistry

SAM	Voc (V)	Jsc (mA/cm²)	FF (%)	PCE (%)	R_s ($\Omega \cdot cm^2$)	R_{sh} ($\Omega \cdot cm^2$)
None	0.61	9.8	46.9	2.8	13	380
C_{60}	0.62	10.6	57.2	3.8	2.4	1010
Terthiophene (TT)	0.60	10.0	56.2	3.4	3.5	880
Benzoic Acid (BA)	0.60	10.5	50.2	3.2	2.7	580
Lauric Acid (LA)	0.61	9.9	49.5	3.0	2.6	440

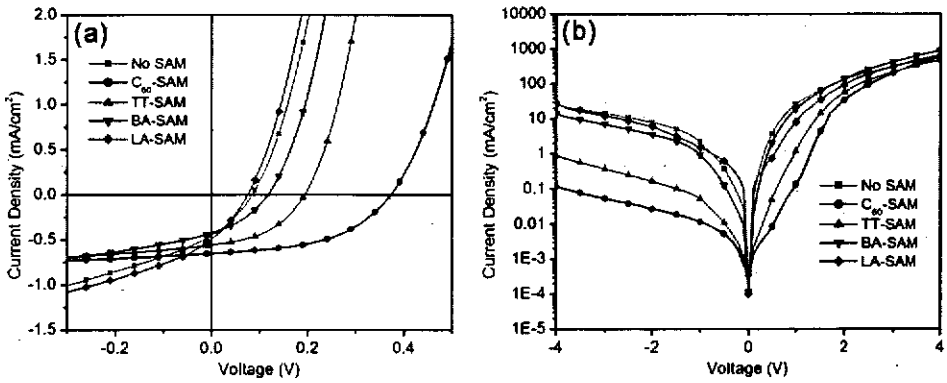

Figure 12. *J-V* characteristics of the inverted P3HT:TiO_2 heterojunction solar cells modified with and without self-assembled monolayers under AM 1.5 illumination (100 mW/cm^2) plotted in linear scale (a) and in the dark plotted in log scale (b). [27]—*Reproduced by permission of The Royal Society of Chemistry.* (Figure available in color online)

losses at the interface and promotes photoinduced charge transfer at the interface. Devices fabricated with the C_{60}-SAM show a low R_s of 2.4 $\Omega \cdot cm^2$ with average device efficiencies of 3.8%.

2.3.1.2 Effect of Self-Assembled Monolayer on Photoinduced Charge Transfer at the Interface. The photo-induced charge transfer property at the inorganic/SAM/organic interface is investigated by fabricating heterojunction TiO_2/P3HT devices. In this device configuration, the only exciton dissociation site is at the n-type TiO_2/p-type P3HT interface. Therefore, the effect of the SAM on the exciton dissociation efficiency can be independently studied with this type of device. The *J-V* plots and the device performance of the heterojunction devices are shown in Fig. 12 and Table 3. The data shows that both the LA-SAM and BA-SAM do not have a significant effect on the device performance whereas the TT-SAM and C_{60}-SAM shows an improvement in all the device characteristics. An improvement in the fill factor and the photocurrent density with the TT-SAM and C_{60}-SAM in this device configuration confirms that photoinduced charge transfer at the interface plays a role in preventing charge back recombination at the TiO_2 interface. Interestingly, the C_{60}-SAM shows the largest improvement in the overall device performance paramters. The reason for this is that the C_{60} molecule is a very good electron acceptor (n-type) under

Table 3

Summary of the average device performance of inverted P3HT:TiO_2 heterojunction solar cells with and without carboxylic acid self-assembled monolayer modification.[27]— Reproduced by permission of The Royal Society of Chemistry

SAM	Voc (V)	Jsc (mA/cm^2)	FF (%)	PCE (%)	Rectification Ratio
None	0.08	0.45	31.5	0.01	4×10^{-2}
C_{60}	0.37	0.65	49.1	0.12	3×10^{-4}
Terthiophene (TT)	0.19	0.56	44.1	0.05	2×10^{-3}
Benzoic Acid (BA)	0.12	0.43	35.7	0.02	2×10^{-2}
Lauric Acid (LA)	0.07	0.49	30.6	0.01	4×10^{-2}

illumination due to photoinduced electron transfer from polymer to C_{60}.[60] The improvement of the BHJ blend system can also be partly explained by this photoinduced electron transfer from P3HT to the C_{60}-SAM, since both P3HT and PCBM can be located at this interface. Furthermore, the large rectification ratio $\sim 10^{-4}$ of the C_{60}-SAM modified device at ± 3 V compared to the other SAMs indicates that the C_{60}-SAM serves as an effective hole blocking layer at the interface.

2.3.1.3 Self-Assembled Monolayer Effect on P3HT Polymer Crystallinity. The effect of the SAM modification on the overlayer crystallinity of the P3HT:PCBM BHJ blend was studied by XRD. The X-ray diffraction spectrum of the bulk-heterojunction blend prior to and after annealing at 150°C on devices with and without SAMs modification are shown in Fig. 13. The diffraction spectrum shows a typical P3HT (100) intensity peak in which the intensity differs depending on the SAM and whether the BHJ was annealed. An overall increase in diffraction intensity is observed in the BHJ films after thermal annealing which is a typical observation of better P3HT ordering. The P3HT diffraction intensity of devices modified with BA-SAM are lower than those without a monolayer showing a negative influence on the overlayer crystallinity implying that improved device performance from the BA-SAM is attributed mainly to the improved charge transfer and lower contact resistance at the interface. The TT-SAM devices show an increase in P3HT diffraction signal indicating that the improvement in crystallinity in addition to the better charge transfer properties at the interface lowers contact resistance and improves the device efficieny. Diffraction signals of the LA-SAM are higher, indicating better P3HT ordering; however, the device efficiencies are poor. The improved order is due to the long alkyl chain SAM interacting with P3HT to help order the P3HT chains.[61] The slight improvement in performance is due to the improved crystallinity of the BHJ film which lowers the series resistance of the device. This improvement is not likely to be due to improved charge transfer at the interface since lauric acid is not electroactive and will act as a physical barrier that affects the electronic coupling between the polymer and TiO_2. C_{60}-SAM modified devices

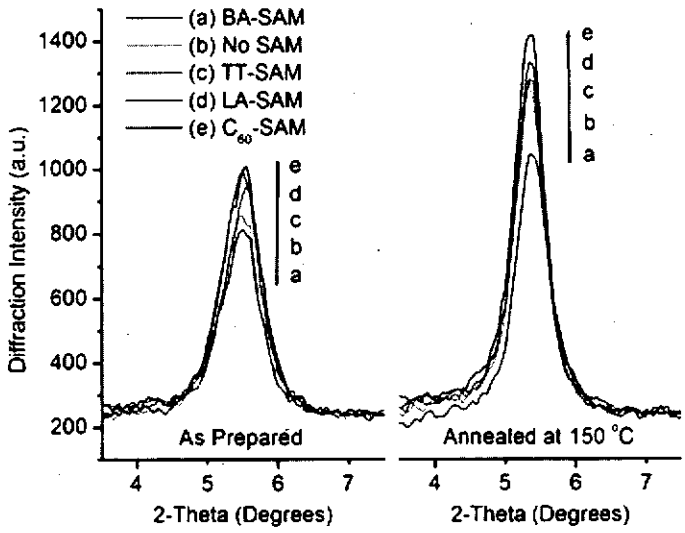

Figure 13. X-ray diffraction spectrum of the P3HT (100) peaks before and after thermal annealing at 150°C on bulk-heterojunction devices modified with and without the SAM.[27]—*Reproduced by permission of The Royal Society of Chemistry.* (Figure available in color online)

show the largest increase in the diffraction signal confirming that it can affect the overlayer crystallinity and morphology. The combined improvements in P3HT crystallinity, contact resistance by passivating surface traps, and photo-induced charge transfer to reduce back charge recombination are reasons for the high performance of these devices.

2.3.1.4 Capacitance-Voltage and Field Effect Transistor Measurements on BHJ Films. The effect of the C_{60}-SAM on the interface between the organic active and inorganic TiO_2 layer can be studied with organic field effect transistors (OFET) and capacitance-voltage (C-V) measurements. C-V and OFET measurements of P3HT:PCBM films can give information regarding the distribution and vertical concentration gradients of the organic materials close to the interface.[62] The transport properties in OFETs are generally determined by the first few nanometers of the active material close to the interface, therefore if one of the two components of the blend segregates towards the bottom interface, the charge carrier mobility should ideally reach its pristine value. OFETs were fabricated of the pristine films of P3HT and PCBM as well as P3HT:PCBM blend films with and without C_{60}-SAM modification on a TiO_2/SiO_2/doped-Si substrate. The transfer characteristics of the pristine films of P3HT and PCBM are given in (Fig. 14(a)) showing a hole mobility of 1.8×10^{-4} $cm^2/V{\cdot}s$ for P3HT and an electron mobility of 1.2×10^{-4} $cm^2/V{\cdot}s$ for PCBM. BHJ blend films without SAM modification had a hole mobility of 4.1×10^{-5} $cm^2/V{\cdot}s$ and an electron mobility of 9.4×10^{-6} $cm^2/V{\cdot}s$. The higher hole mobility compared to the electron mobility indicates that a higher concentration of P3HT is accumulated at the interface which is in agreement with previous reports of blend films cast from di-chlorobenzene showing higher concentrations of P3HT near the bottom interface.[63] However, BHJ films with C_{60}-SAM modification show a hole mobility of 1.8×10^{-5} $cm^2/V{\cdot}s$ and an electron mobility of 1.0×10^{-4} $cm^2/V{\cdot}s$. The electron mobility in this case is higher than the hole mobility confirming that more PCBM is accumulated at the interface. To further confirm this, C-V measurements (Fig. 14(b)) also indicate that the C_{60}-SAM facilitates the accumulation of PCBM to the bottom TiO_2 interface. The C_{60}-SAM modified devices show p-mode and n-mode accumulation that is in agreement with what was found from the OFET measurements. C-V measurements of devices without the SAM show higher capacitance under negative gate voltage implying a more p-mode accumulation at the interface and

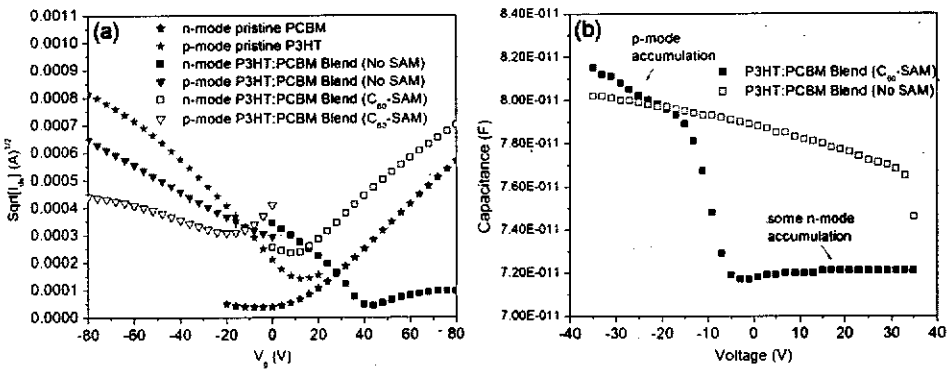

Figure 14. (a) Square-root of the measured transfer characteristics of OFETs prepared from the pristine P3HT, PCBM and blend films of P3HT:PCBM (weight ratio 1:0.8) with and without C_{60}-SAM modification at the TiO_2 interface. (b) Capacitance-voltage measurement of blend films of P3HT:PCBM (weight ratio 1:0.8) with and without C_{60}-SAM modification at the TiO_2 interface.[27]— *Reproduced by permission of The Royal Society of Chemistry.* (Figure available in color online)

show that no significant n-mode accumulates under positive gate bias. The C_{60}-SAM can help to nucleate PCBM to provide a better percolation conduction pathway of PCBM at the interface to improve the overall distribution of phases, morphology, and crystallinity of the blend leading to better charge selectivity. The C_{60}-SAM leads to a 35% improvement in device PCE over unmodified TiO_2 inverted devices. Understanding how to reduce the interface and bulk-heterojunction resistance in a PV cell is critical in reducing losses in PV performance caused by a recombination of charge carriers.

2.3.2 Inverted Solar Cells: Modification of ZnO Electron Selective Layers with Self-Assembled Monolayers. The high electron mobility of ZnO compared to titanium oxide makes it a better electron selective contact layer for inverted solar cells due to the lower resistances. However, interface resistances caused by charge traps attributed to the hydroxylated ZnO surface can still lead to a high charge carrier recombination; therefore, modification of the surface with a SAM is still necessary. The ZnO inverted device architecture and structure of the C_{60}-SAM are shown in Fig. 15. The *J-V* characteristics of the bulk-P3HT/PCBM heterojunction (BHJ) and P3HT/ZnO heterojunction (HJ) inverted devices with and without C_{60}-SAM modification and device performance parameters are shown in Fig. 16 and Table 4. BHJ devices without SAM modification had an average power conversion efficiency (PCE) of ~3.7%. The performance of the inverted solar cell is improved by modifying the ZnO surface with a C_{60}-SAM. The PCE is improved by over 20% compared to the unmodified devices giving an average PCE of 4.5% and the highest PCE of 4.9%. An improvement in both the FF from 55.4% to 60.6% and J_{sc} from 10.8 mA/cm^2 to 12.0 mA/cm^2 is observed after modification with the C_{60}-SAM. This improvement is attributed to better electronic coupling of the inorganic/organic interface from the C_{60}-SAM through the process of photo-induced charge transfer as similarly observed in the TiO_2 based C_{60}-SAM modified inverted devices. This helps mediate forward charge transfer and reduces the back charge recombination at the interface leading to improved photocurrent and charge selectivity.

Bilayer heterojunction devices of ZnO modified with and without the C_{60}-SAM and pristine P3HT were fabricated showing an almost two times improvement in power conversion efficiency in the C_{60}-SAM devices over unmodified HJ devices. An improvement in both the FF and J_{sc} from 46.7% to 54.2% and from 1.1 mA/cm^2 to 1.8 mA/cm^2 is observed. A lower V_{oc} is observed with the C_{60}-SAM modified devices as compared to the unmodified device due to the fact that exciton dissociation happens at the C_{60}-SAM/P3HT

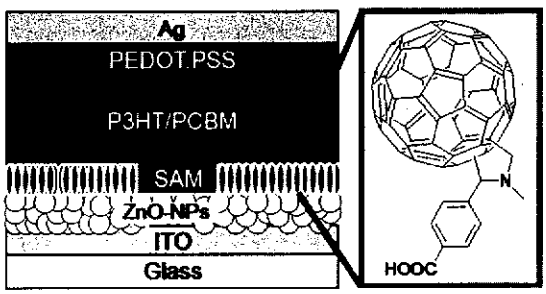

Figure 15. Device structure and chemical structure of ZnO-NPs based inverted solar cell with C_{60}-SAM modification. Adapted with permission from.[24] Copyright 2008 American Institute of Physics. (Figure available in color online)

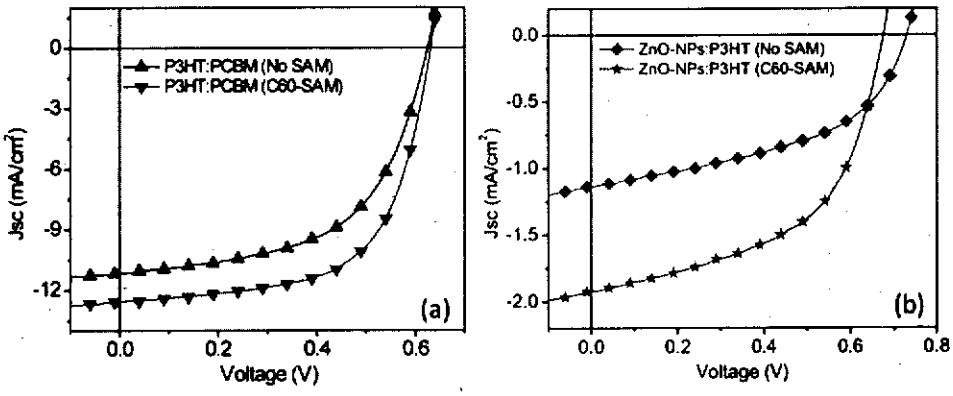

Figure 16. (a) *J-V* characteristics of inverted ZnO NP/P3HT:PCBM bulk-heterojunction solar cells with and without C_{60}-SAM modification. (b) *J-V* characteristics of inverted ZnO NP/P3HT heterojunction solar cells with and without C_{60}-SAM modification. Adapted with permission from.[24] Copyright 2008 American Institute of Physics. (Figure available in color online)

interface and not the ZnO/P3HT interface. It is known that the V_{oc} between fullerenes and P3HT is typically less than 0.7 V while between ZnO and P3HT can be greater than 0.7 V.[64] Figure 17 shows the results of the external quantum efficiency (EQE) measurements on the BHJ and HJ devices modified with and without the C_{60}-SAM. The EQE for the BHJ devices without modification shows a maximum of ~49% at 500 nm while after C_{60}-SAM modification, the EQE reaches ~70%. A similar trend is observed with the HJ devices showing an increase in EQE from ~11% to 17% after modification with the C_{60}-SAM.

2.4 Processing Optimization of the BHJ Active Layer for Inverted Polymer Solar Cells

The processing conditions of the active layer film can have a dramatic effect on the final device efficiency. The processing conditions of the blend films that can affect the device efficiency are the blend ratio of donor and acceptor materials, the active layer film thickness, the thermal annealing temperature, and the thermal annealing time. By varying these processing conditions in C_{60}-SAM modified inverted solar cells, it is found that the optimum active layer efficiency is ~4.5% using a P3HT:PCBM blend ratio of 1:0.7, an active layer thickness of ~200 nm at an annealing temperature and time of 160°C for 10 min.[65]

Table 4

Summary of the average device performance of inverted ZnO-NPs/P3HT:PCBM bulk-heterojunction solar cells and ZnO-NPs/P3HT heterojunction solar cells with and without C_{60}-SAM modification. Adapted with permission from.[24] Copyright 2008 American Institute of Physics

Active Material	SAM	Voc (V)	Jsc (mA/cm^2)	FF (%)	PCE (%)
P3HT:PCBM	None	0.63	10.8	55.4	3.7
P3HT:PCBM	C_{60}	0.63	12.0	60.6	4.5
P3HT	None	0.75	1.08	46.7	0.37
P3HT	C_{60}	0.67	1.83	54.2	0.67

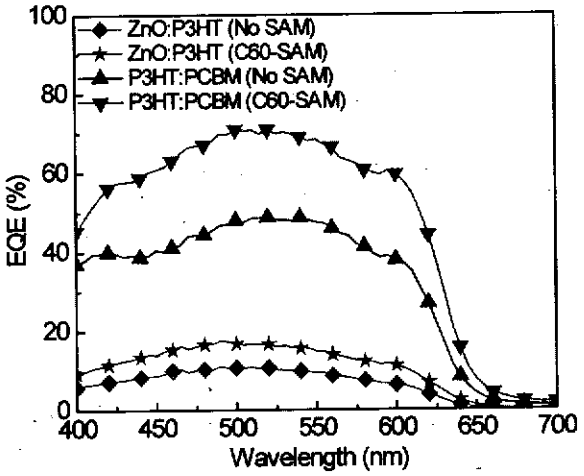

Figure 17. External quantum efficiencies of ZnO-NPs/P3HT:PCBM bulk-heterojunction and ZnO-NPs/P3HT heterojunction inverted solar cells with and without C_{60}-SAM modification. Adapted with permission from.[24] Copyright 2008 American Institute of Physics. (Figure available in color online)

2.4.1 BHJ Donor/Acceptor Ratio Dependence on Performance of Inverted Solar Cells. The ratioFigure 17 of donor and acceptor materials in BHJ blends influence the size and distribution of phases leading to changes in the number of interfaces for exciton dissociation and charge carrier transport. Reduction in the donor and acceptor interfaces lowers the probability for exciton dissociation while increasing the probability for charge carrier recombination due to the lower mobilities of organic materials. A balanced electron and hole charge transport throughout the blends minimizes these recombination occurrences and improves the solar cell performance. Generally, the ratio of P3HT: PCBM that has been found to have high efficiencies in the conventional architecture in the range of 1:0.8 to 1:1.

Table 5 and Fig. 18 summarize the results of the inverted devices with and without the C_{60}-SAM modification varying the blend ratios keeping the annealing temperature and time at 160°C and 10 min. Devices fabricated without PCBM (P3HT/ZnO-NPs heterojunctions) show a PCE of 0.2%, but when modified with a C_{60}-SAM, the PCE is improved to 0.3% due to the improvement in J_{sc} and FF. The improvement in FF and J_{sc} in the C_{60}-SAM devices is attributed to the improved charge transfer properties from P3HT to ZnO. The resistance at the ZnO interface dominates the device parameters since the only interface for exciton separation is at the polymer/ZnO-NPs interfaces. Devices with P3HT:PCBM ratios of 1:0.1, 1:0.2, and 1:0.3 show similar FF for both the C_{60}-SAM modified and unmodified devices. The similar FF of both modified and unmodified devices indicates that the active layer now dominates the resistances in the solar cell. The V_{oc} for the unmodified devices are low (0.33 V, 0.38 V, 0.49 V) compared to ones modified with the C_{60}-SAM (0.41 V, 0.50 V, 0.58 V) in these blend ratios. The addition of the PCBM into the BHJ blend adds additional interfaces that also play a role in determining the V_{oc}. The low concentration of PCBM in these blends may not provide a good morphology and percolation pathway thus leading to low V_{oc}. At the blend ratio of 1:0.4 (~29% PCBM content), the resistances in the bulk active layer (donor-acceptor) and across the interfaces (ZnO) are comparable, thus changes at ZnO interfaces can have a major effect on the solar cell performances. However, the V_{oc} of devices are independent of ZnO modification indicating that the amount of

Table 5

Average device performance of inverted ZnO-NPs/P3HT:PCBM bulk-heterojunction solar cells fabricated with different active layer blend weight ratios from 1:0 to 1:1 (w:w). Parentheses indicate average device performance of inverted solar cells modified with the C_{60}-SAM. Adapted with permission from.[65] ©2010EEE

Ratio	Voc (V)	Jsc (mA/cm^2)	FF (%)	PCE (%)
1:0	0.60 (0.43)	0.5 (1.2)	48.7 (52.6)	0.2 (0.3)
1:0.1	0.33 (0.41)	1.3 (1.8)	46.6 (47.2)	0.2 (0.4)
1:0.2	0.38 (0.50)	2.2 (3.4)	44.8 (44.4)	0.4 (0.8)
1:0.3	0.49 (0.58)	4.5 (6.2)	43.6 (43.9)	1.0 (1.6)
1:0.4	0.63 (0.64)	9.0 (10.3)	47.7 (52.2)	2.7 (3.5)
1:0.5	0.63 (0.64)	10.6 (10.8)	55.6 (60.0)	3.7 (4.1)
1:0.6	0.63 (0.63)	10.8 (11.0)	59.5 (61.8)	4.0 (4.3)
1:0.7	0.62 (0.62)	10.6 (11.2)	60.8 (64.2)	4.0 (4.5)
1:0.8	0.62 (0.62)	10.5 (10.8)	62.2 (64.8)	4.1 (4.3)
1:0.8	0.61 (0.61)	10.1 (10.2)	62.9 (65.2)	3.9 (4.1)
1:1	0.61 (0.62)	10.0 (10.3)	62.5 (62.6)	3.8 (4.0)

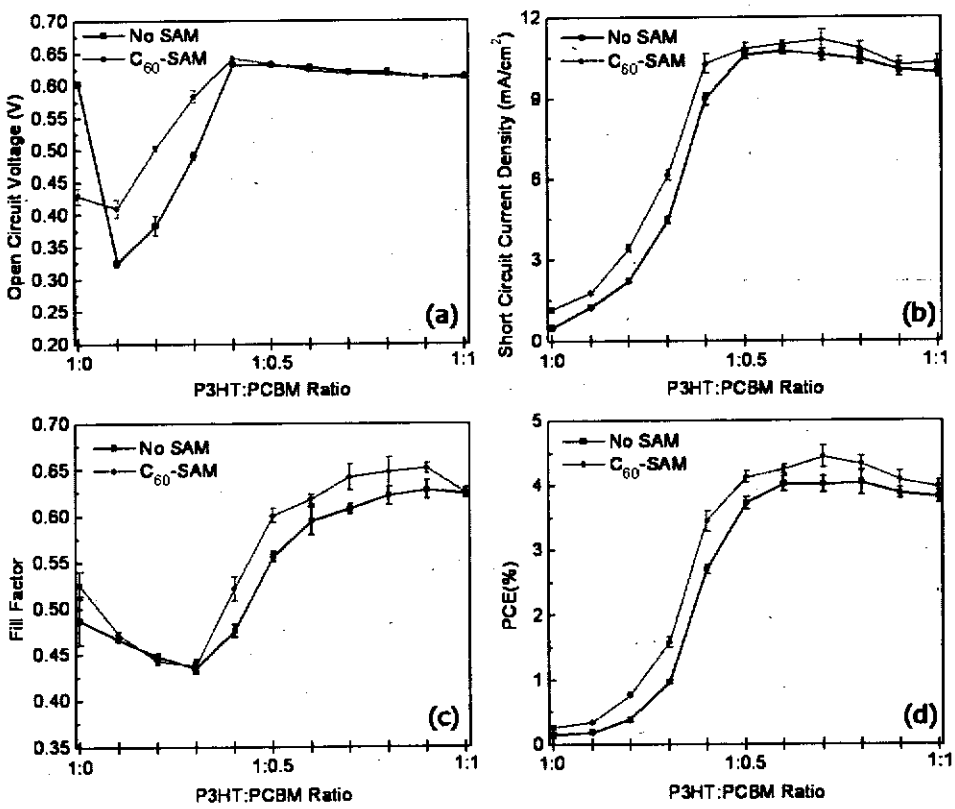

Figure 18. Plots of the four device parameters (a) V_{oc}, (b) J_{sc}, (c) FF, and (d) PCE as a function of P3HT:PCBM blend ratio (w:w) (from 1:0 to 1:1) in inverted ZnO-NPs/P3HT:PCBM solar cells with and without C_{60}-SAM modification. Adapted with permission from.[65] ©2010EEE. (Figure available in color online)

blend P3HT:PCBM interfaces are large enough to lead to good distribution of phases to minimize charge recombination. Increasing the ratio from 1:0.3 to 1:0.4, the efficiency increases from 1.0% to 2.7% in unmodified devices and from 1.6% to 3.5% in C_{60}-SAM modified devices. The unmodified devices still show low fill factor and J_{sc} (47.6%, 9.0 mA/cm^2) indicating resistances in the solar cell, but after modification with a C_{60}-SAM, the fill factor and J_{sc} are improved to 52.2% and 10.3 mA/cm^2. This shows that the SAM is influencing the blend active layer morphology and reducing the resistance losses caused from carrier recombination. Increasing the blend ratio from 1:0.5 to 1:1 show saturation in the device V_{oc} in both the modified and unmodified devices. The C_{60}-SAM devices at higher blend ratios show improvements in J_{sc} and FF compared to devices without modification. The highest PCE reached ~4.5% at blend ratios of 1:0.7. At these ratios, the C_{60}-SAM effect on the bulk morphology to improve solar cell efficiency is minimized. Therefore, the improvement from the C_{60}-SAM at these higher ratios is mainly due to the improved charge transfer properties at the interface.

2.4.2 Influence of BHJ Film Thickness on Inverted Solar Cell Performance. Another parameter that can influence the performance of the inverted solar cell is the BHJ film thickness. Inverted solar cells from solution concentrations of 10 mg/mL to 60 mg/mL were spun at 1500 rpm and its effect on the four device parameters are show in Fig. 19. The optimization of the BHJ film thickness in these inverted solar cells utilized a blend ratio of 1:0.7 and an annealing condition of 160°C for 10 min. The V_{oc} using a 10 mg/mL concentration is low ~0.53 V, but as the solution concentration increases (increasing film thickness), the V_{oc} increases and remains similar ~0.61–0.63 V. The lower V_{oc} in the thin layer may be attributed to the formation of more current leakage pathways in the film causing higher recombination of charges. As the BHJ film thickness is increased, the J_{sc} also increases due to the higher optical absorbance of the film generating more charge carriers. With a thin BHJ film (10 mg/mL), the FF is very poor, but increasing the film thickness leads to fill factors greater than 60%. However, increasing the thickness further leads to a decrease in fill factor due to the high resistance of the active layer from the poor charge carrier transport of the organic materials. In the ideal case, the BHJ film thickness should both maximize photon absorbance and still maintain high carrier mobility to allow maximum collection of the charges. It is found that the BHJ film thickness of ~200 nm (40 mg/mL) shows the optimum PCE in these inverted solar cells.

2.4.3 Influence of Thermal Annealing Temperature on the Performance of Inverted Solar Cells. Another processing parameter that can influence the performance of solar cells is the thermal annealing of the BHJ blend. Annealing can change the blend morphology and segregation of donor/acceptor phases which can influence the number of interfaces for exciton dissociation. The device performance of inverted solar cells with thermal annealing temperatures from 100–200°C using a BHJ film thickness of ~200 nm, a blend ratio of 1:0.7 and an annealing time of 10 min were studied (Fig. 20). The annealing temperature showed very minimal effect on V_{oc} until 200°C where it decreased to ~0.57 V. The annealing temperature shows a maximum J_{sc} in devices with annealing temperatures ~130°C to 160°C. Increasing the annealing temperature further leads to a lowering of the J_{sc}. The FF however shows a dramatic change with annealing temperature. Temperatures below 120°C lead to fill factors below 50%. Further increasing the temperature from 130°C to 170°C leads to fill factors as high as 65%. However, increasing temperatures beyond 170°C leads to a reduced fill factor. This drastic change in the fill factor is explained by the evolution of the blend morphology as characterized by AFM (Fig. 21). Low annealing temperatures are

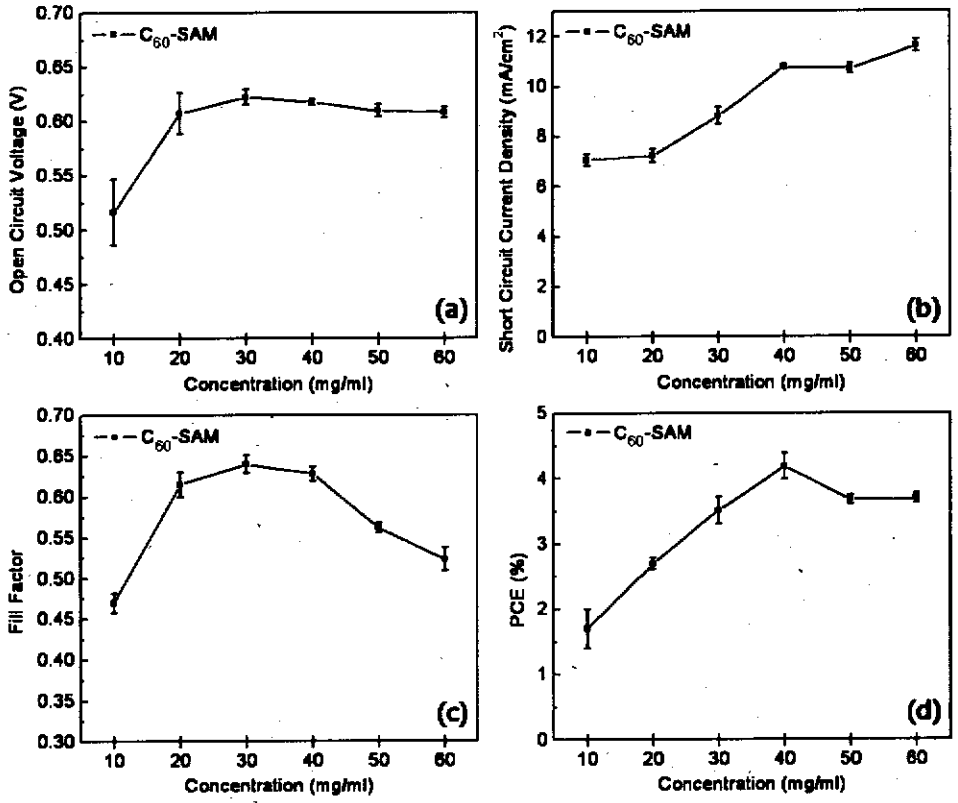

Figure 19. Plots of the four device parameters (a) V_{oc}, (b) J_{sc}, (c) FF, and (d) PCE as a function of solution concentration of P3HT:PCBM blends spincoated at 1500 rpm (changes in thickness of active layer) in inverted ZnO-NPs/ C_{60}-SAM/P3HT:PCBM solar cells. Adapted with permission from.[65] ©2010EEE.

insufficient to allow the P3HT and PCBM to interact strongly which causes poor mobility in the phases of the organic materials leading to high carrier recombination. At elevated temperatures (130°C to 160°C), the thermal energy required for both the P3HT and PCBM to pack and interact is sufficient to allow the phases to segregate into the optimum nanophase morphology. At higher temperatures (170°C to 200°C), the size of the phases begin to grow as indicated by the AFM images. These larger phases lower the number of interfaces for exciton dissociation causing higher charge carrier recombination therefore decreasing the J_{sc} and FF. The optimum annealing temperature leading to the PCE is at 160°C.

2.4.4 Influence of Thermal Annealing Time on the Performance of Inverted Solar Cells. In addition to the annealing temperature, the annealing time can also influence the final performance of polymer-based solar cells. Based on previously optimizing the BHJ blend ratio, BHJ film thickness, and annealing temperature device using a blend ratio of 1:0.7, thickness ~200 nm, and annealing temperature ~160°C were studied. The BHJ layers were varied from no annealing to 60 min of thermal annealing as shown in Fig. 22. Inverted devices without annealing and annealed for 60 mins show changes in V_{oc} from ~0.60 V to 0.62 V and J_{sc} from 9.5 mA/cm^2 to 10.3 mA/cm^2. The fill factor is found to be sensitive to the annealing time having fill factors lower than 45% when the active layer

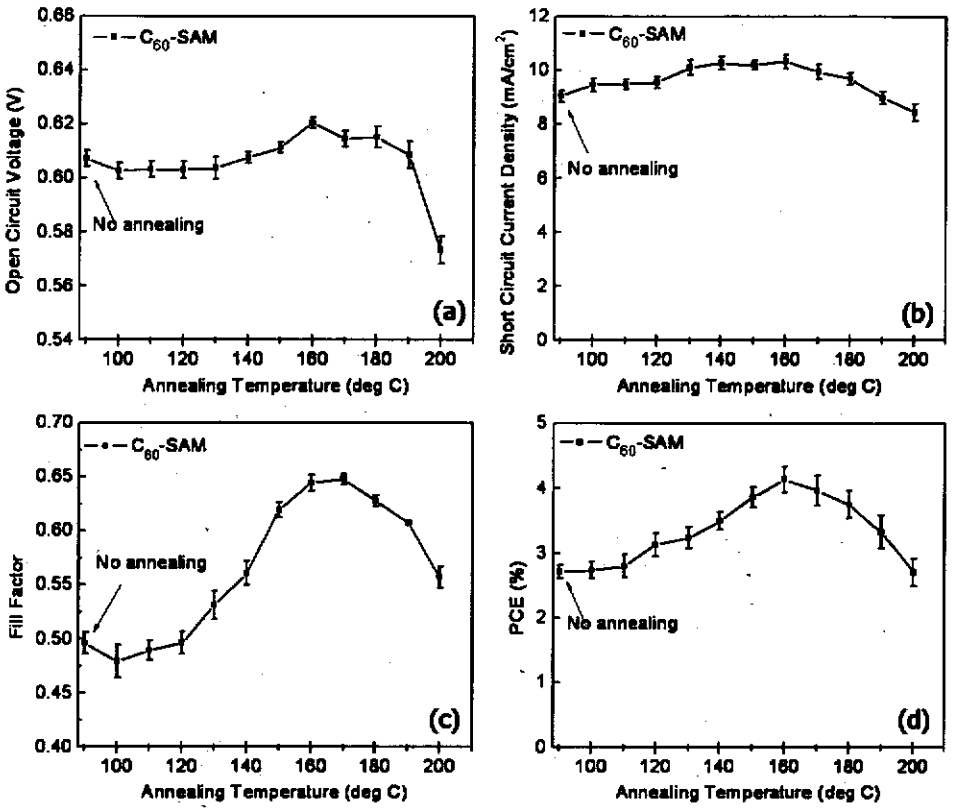

Figure 20. Plots of the four device parameters (a) V_{oc}, (b) J_{sc}, (c) FF, and (d) PCE as a function of thermal annealing temperatures of P3HT:PCBM blends from no annealing to 200°C in inverted ZnO-NPs/ C_{60}-SAM/P3HT:PCBM solar cells. Adapted with permission from.[65] ©2010EEE.

is not annealed. After 1 min of annealing, the fill factor increases to ~57% and further increases to over 65% after 5 mins of thermal annealing. With 10 mins of annealing, the PCE showed optimum performance with efficiencies over 4%. Annealing for longer times (60 min) show very little change in efficiency when compared to devices annealed at 10 min indicating that shorter annealing times at a annealing temperature of 160°C is sufficient to optimize the BHJ blend morphology. Optimizing the processing conditions for the BHJ active layer allows understanding of the processing control required to maintain high device performances for potential large-scale production of these inverted based solar cells.

2.5 Optimization of Electrodes in Inverted Polymer Solar Cells

2.5.1 Influence of the Top Metal Anode Electrode on the Performance of Inverted Polymer Solar Cells. The performance of polymer-based solar cells can also be influenced by the nature of charge collection at the interface of the active layer and electrode. For a single component diode, the metal-insulator metal (MIM) model suggests that the V_{oc} is given by the difference between the work functions of the anode and cathode.[66,67] This holds as long as one or both of the contacts is non-Ohmic in nature. If the work function of either electrode coincides with or is smaller than the LUMO or greater than the highest occupied

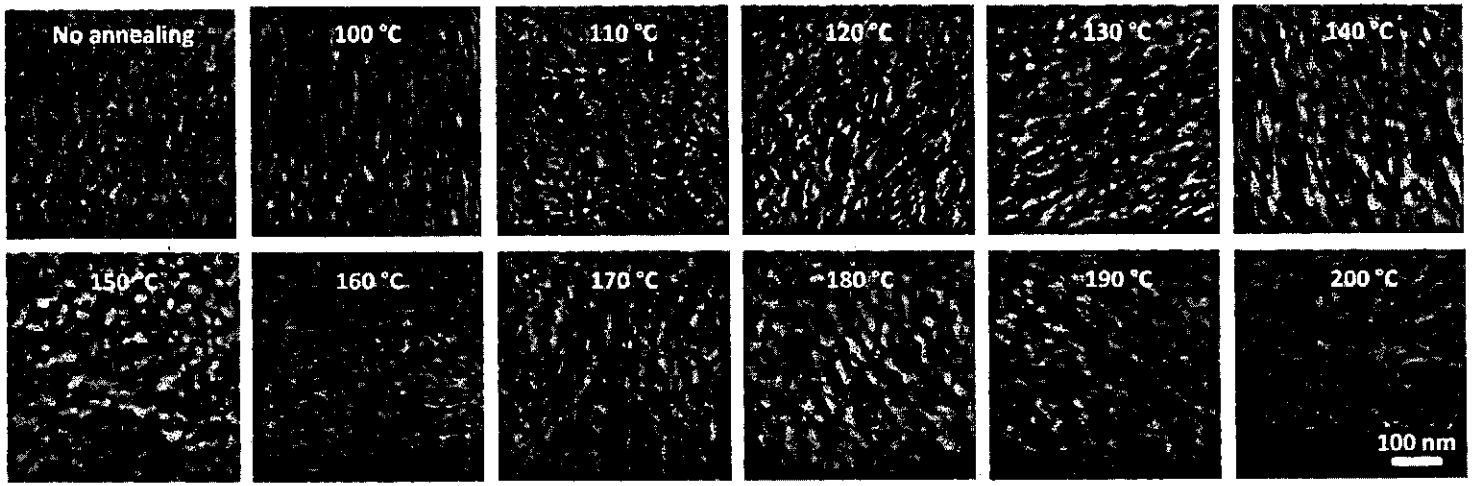

Figure 21. AFM images of thermally annealed inverted ZnO-NPs/ C_{60}-SAM/P3HT:PCBM solar cells blends from no annealing to 200°C with the PCBM phase removed by 1,8-octanedithiol. Images show an evolution of the P3HT phases into larger phases with higher annealing temperatures. The scan size for the AFM images are 0.5 μm × 0.5 μm. Adapted with permission from.[65] ©2010EEE. (Figure available in color online)

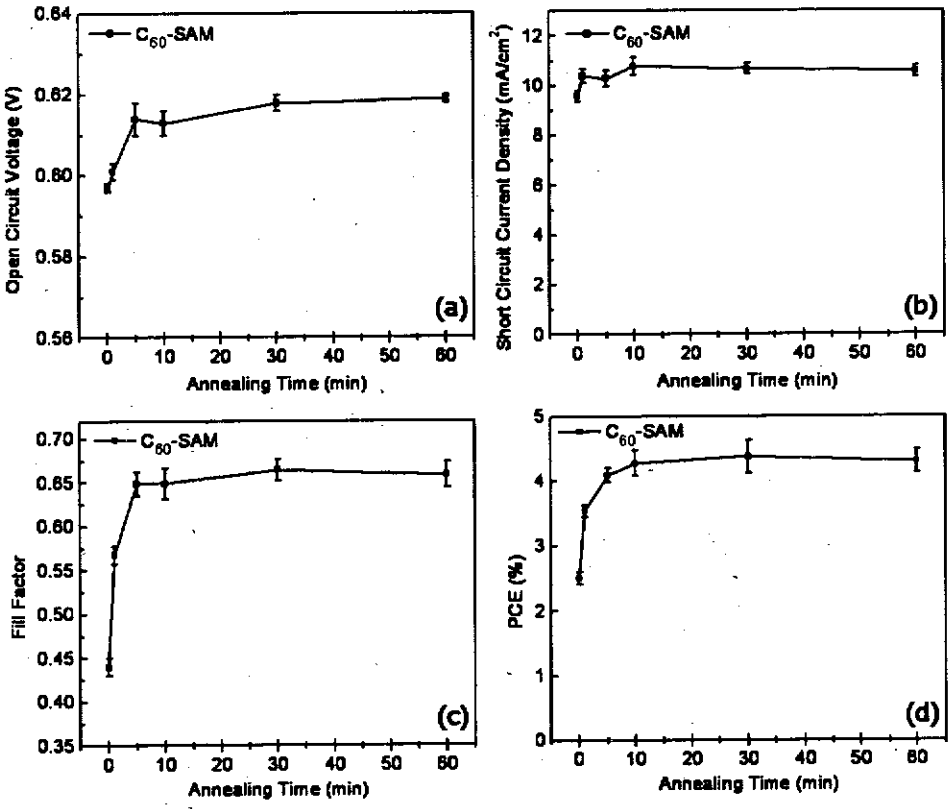

Figure 22. Plots of the four device parameters (a) V_{oc}, (b) J_{sc}, (c) FF, and (d) PCE as a function of thermal annealing time of P3HT:PCBM blends from no annealing to 60 min annealing in inverted ZnO-NPs/ C_{60}-SAM/P3HT:PCBM solar cells. Adapted with permission from.[65] ©2010EEE.

molecular orbital (HOMO) of the semiconductor, the Fermi level of that electrode pins at the appropriate energy level. Under these conditions, the V_{oc} cannot exceed the band-gap of the polymer. However, with the incorporation of an electron acceptor material in a BHJ system, V_{oc} is limited to the difference between the HOMO of the donor and the LUMO of the acceptor.

Different top metal contacts for inverted solar cells are examined and the device characteristics are summarized in Table 6. Device fabricated with the top anode electrode using Ag, Cu, Au, and Pd show very similar PCE and almost no change in V_{oc}. However, with inverted devices fabricated with Al and Ca/Al show a lower PCE. The J_{sc} of the Al and Ca/Al devices were 6.7 and 0.2 mA/cm^2, respectively. These values are much lower than the devices using higher work function electrodes which had average Jsc of ~10 mA/cm^2. X-ray photoelectron spectra show that Al reacts to form chemical bonds with the sulfonic acid moiety of PEDOT:PSS [68] resulting in a thin insulating layer. Calcium is also susceptible to moisture and likely oxides very rapidly in air leading to similar interfacial degradation. Higher work function electrodes such as Au and Pd show inverted solar cell efficiencies of 3.9% and 3.8%, respectively. The best device in this series of electrodes uses Ag as the anode with average efficiencies over 4%. Interestingly, Cu as an anode electrode also shows similar device performance having efficiencies of 3.8%. The data demonstrates

Table 6
Average device performance of inverted ZnO-NPs/P3HT:PCBM bulk-heterojunction solar cells fabricated with different top metal electrodes. Adapted with permission from.[65] ©2010EEE

Anode Electrode	Voc (V)	Jsc (mA/cm^2)	FF (%)	PCE (%)
Pd	0.63	9.7	61.9	3.8
Au	0.62	10.2	61.7	3.9
Cu	0.62	10.0	61.6	3.8
Ag	0.62	10.3	62.3	4.0
Al	0.61	6.7	60.5	2.5
Ca/Al	0.61	0.2	46.2	0.1

that given the proper device architecture, even inexpensive electrodes can be utilized to generate high efficiency solar cells. This has implications for reducing fabrication cost for large-scale fabrication of polymer-based solar cells.

2.5.2 Solution Processed, Vacuum-Free Electrodes for Inverted Polymer Solar Cells.

2.5.2.1 Silver Nanoparticles as the Top Metal Anode in Inverted Polymer Solar Cells. Ideally, all the processing of the active layers and electrodes as well as encapsulation should be done under ambient conditions. However, this cannot be achieved with the typical conventional architecture which requires both high vacuum for metallization and an inert environment for encapsulation to produce the final solar cell. The inverted architecture has been shown previously to maintain high efficiency even with the use of higher work function electrodes. These higher work function metal electrodes like Ag can be done by printing and coating techniques which can be easily integrated into the roll-to-roll type processing. In our inverted device architecture, PEDOT:PSS is utilized between the active layer and the top metal electrode. Because PEDOT:PSS provides a good protective layer to the active layer, a method was developed to process solution processible Ag-nanoparticles as the top metal electrode in inverted solar cell devices.

The top metal electrode in these inverted solar cell devices was processed by spray-coating a solution of the Ag-nanoparticles through a mask to define the device area. The spraycoating process and final coating can be controlled by changing variables including the solution viscosity, spray pressure, the spray distance from sample, spray time, and the number of spray coats. In this study, the variables other than the number of coats were held constant. The *J-V* characteristics and device performance parameters for the different number of Ag-nanoparticle coating layers is shown in Fig. 23 and Table 7. Devices with a coating of 20 layers show a low J_{sc} of 7.7 mA/cm^2, FF of 44.5%, and PCE of 2.1%. Increasing the coating layer to 100 coats shows a saturation of J_{sc} to 8.3 mA/cm^2. A significant improvement in the FF is observed from 20 coats (44.5%) to 100 coats (59.6%) which are attributed to the reduced resistance of the Ag-nanoparticle electrode with the thicker coating. Devices fabricated with the 100 layer coating of the Ag-nanoparticles show an average device efficiency of ~3.0%. Devices using a vacuum deposited Ag electrode have a J_{sc}, FF, and PCE of 9.3 mA/cm^2, 62.2% and 3.6% respectively. The Ag spraycoated electrode has a 0.6% difference in PCE compared to the device with the evaporated Ag electrode.

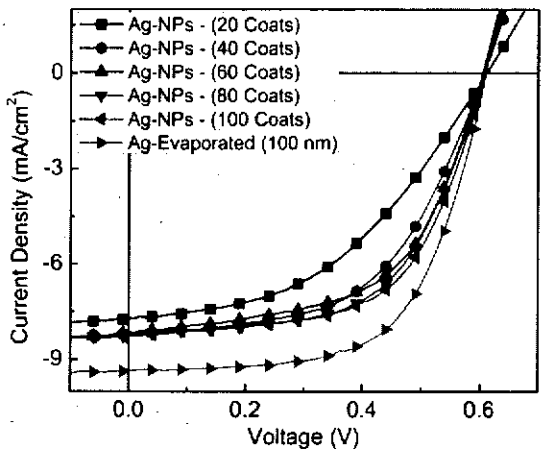

Figure 23. Illuminated *J-V* characteristics of inverted ZnO NP/C_{60}-SAM/P3HT:PCBM bulk-heterojunction solar cells fabricated on glass/ITO by spraycoating Ag-NPs (from 20–100 coats) or evaporating Ag as the anode electrode. Adapted with permission from.[14] Copyright 2009 Elsevier. (Figure available in color online)

Electrical (four-point probe) and optical (UV-Vis, SEM) characterization of the Ag spraycoated and Ag evaporated electrodes were compared to rationalize the reason for the differences in efficiency. Electrical four-point probe measurements and optical SEM images on a 20 layer coating show a poor Ag-nanoparticle interconnectivity which is the reason for the low efficiency from these devices (Fig. 24(b)). Increasing the layer coating to 40 gave a sheet resistance of 7.55 Ω/sq while further increasing it to 100 lead to a sheet resistance of 0.71 Ω/sq which is comparable to the evaporated electrode (0.51 Ω/sq). The lower sheet resistance from the 100 coating layer of the Ag-nanoparticles is the reason for the similar fill factors in both the Ag spraycoated and Ag evaporated electrodes. This still does not explain the difference in efficiency between the 100 layer coating and Ag evaporated electrode. To

Table 7

Average device performance of inverted ZnO NP/C_{60}-SAM/P3HT:PCBM bulk heterojunction solar cells fabricated on glass/ITO and plastic/ITO substrates by either vacuum deposition of Ag or spraycoating of Ag-NPs as the anode electrode. Sheet resistance of vacuum deposited Ag and different spraycoated Ag-NPs electrodes. Adapted with permission from.[14] Copyright 2009 Elsevier

Electrode Deposition	Voc (V)	Jsc (mA/cm^2)	FF (%)	PCE (%)	Ag Sheet Resistance (Ω/□)
Vacuum	0.61	9.3	62.2	3.6	0.51
Vacuum (Plastic)	0.61	8.3	34.3	1.7	–
Spraycoat (20 coats)	0.61	7.7	44.5	2.1	–
Spraycoat (40 coats)	0.61	8.2	54.2	2.7	7.55
Spraycoat (60 coats)	0.61	8.2	56.6	2.8	3.47
Spraycoat (80 coats)	0.61	8.2	58.1	2.9	1.84
Spraycoat (100 coats)	0.61	8.3	59.6	3.0	0.71
Spraycoat (100 coats) (Plastic)	0.60	6.9	34.0	1.4	–

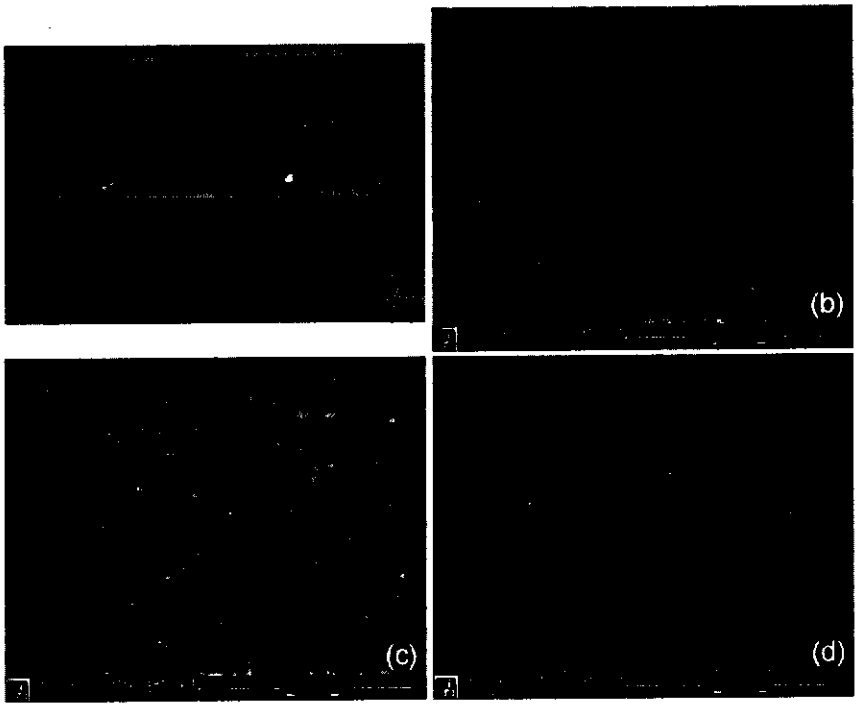

Figure 24. (a) Photograph of polymer solar cells using an Ag spraycoated electrode (left) and Ag evaporated electrode (right). SEM images of (b) spraycoated Ag-NPs (20 coats) after annealing at 120°C for 5 min; (c) spraycoated Ag-NPs (100 coats) after annealing 120°C for 5 min; (d) 100 nm evaporated Ag. Scale bar: 200 nm. Adapted with permission from.[14] Copyright 2009 Elsevier. (Figure available in color online)

explain the reduced efficiency, UV-Vis measurements were performed on the electrodes in the range from 300–800 nm. The transmission near the P3HT absorbance peak (~550 nm) of the different layer coatings show a transparency of ~45% for a 20 layer coating (Fig. 25). After increasing the layer coating to 80 and 100, the transmission at 550 nm is reduced to ~12% and ~9%, respectively. These values are still higher than the evaporated Ag film at 550 nm which is ~1%. SEM images of the Ag-NPs film with a layer coating of 100 compared to the Ag evaporated film show a less dense film morphology (Fig. 24(d)). The smoother and denser Ag evaporated film improves the reflectivity of Ag which improves the photocurrent density of the solar cell. This spraycoating technique was also demonstrated onto flexible ITO substrates showing efficiencies as high as 1.4%. This is comparable to Ag evaporate electrodes on these flexible ITO substrates which showed efficiencies of 1.7%. This approach removes the need to use high vacuum to deposit the top electrode allowing the possibility for roll-to-roll fabrication of solar cells.

2.5.2.2 Indium Tin Oxide-Free Inverted Solar Cells using Conducting Polymers as Electrodes. Indium tin oxide (ITO) has been utilized as the semi-transparent conducting electrode for development of organic solar cell. However, ITO is typically processed at elevated temperatures to improve crystallinity and conductivity, therefore the process is not ideal for flexible roll-to-roll solar cell fabrication. ITO with lower conductivity can be processed onto flexible plastic substrates, but the brittleness of ITO leads to significant degradation in conductivity and device performance due to the formation and propagation

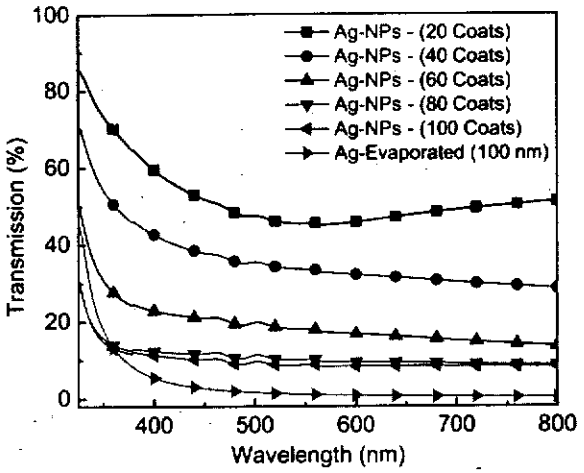

Figure 25. UV-vis transmission spectrum of spraycoated Ag-NPs electrodes from 20 to 100 coats compared to a 100nm Ag evaporated electrode on glass substrates. Adapted with permission from.[14] Copyright 2009 Elsevier. (Figure available in color online)

of cracks. The increasing costs of indium may also prevent large-scale usage of ITO as an electrode material for low-cost polymer-based solar cells. Therefore replacement of ITO as the semi-transparent electrode is needed. A particular organic based electrode material of interest is conducting PEDOT:PSS due to its solution processibility which makes them compatible with the concept of large-scale roll-to-roll processing.

The use of PEDOT:PSS as a semi-transparent electrode to replace ITO is evaluated by measuring both the transparency and sheet resistance of different thicknesses of PEDOT:PSS processed with DMSO (Fig. 26).[69] UV-Vis spectroscopy of various thicknesses

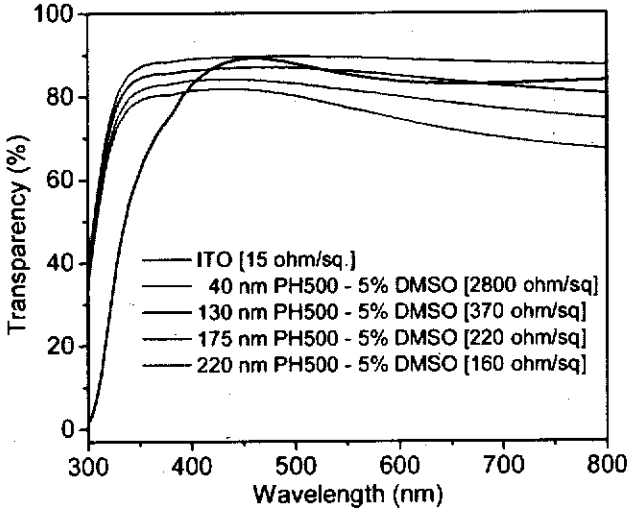

Figure 26. Transparency vs. wavelength of varying thicknesses of PEDOT:PSS −5% DMSO electrodes on glass as compared to transparency of ITO on glass as referenced against air. Legend also indicates corresponding sheet resistances obtained as measured by four-point probe. Adapted with permission from.[69] Copyright 2009 Elsevier. (Figure available in color online)

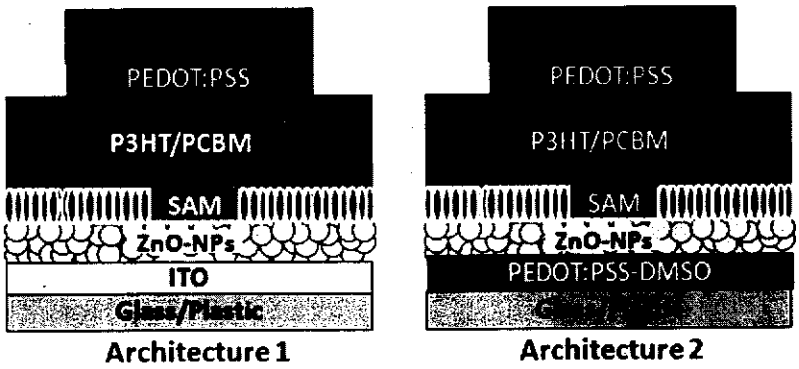

Figure 27. Device architectures of the inverted solar cells with ITO or PEDOT:PSS-DMSO electrodes. Adapted with permission from.[69] Copyright 2009 Elsevier. (Figure available in color online)

of PEDOT:PSS show that a ~130 nm thick PEDOT:PSS layer has comparable transparency to the ITO. The sheet resistance of the PEDOT:PSS layer however, is ~25 times higher than that of ITO (15 Ω/□). Increasing the PEDOT:PSS thickness to ~220 nm leads to a reduction in sheet resistance to as low as 160 Ω/□, but also shows a decrease in transparency due to the absorbance from the PEDOT:PSS film.

Inverted solar cells fabricated with different electrode PEDOT:PSS thicknesses is compared to devices fabricated from ITO. The device configuration of these two architectures is shown in Fig. 27. The *J-V* characteristics and device performance parameters are shown in Fig 28(a) and Table 8. Devices using a thin PEDOT:PSS layer (~40 nm) have an average J_{sc} of 9.6 mA/cm^2, FF of 39.4% and a PCE of 2.3%. A PEDOT:PSS electrode thickness of ~130 nm improved the overall PCE to ~3.1%. However, a lower average J_{sc} of 9.4 mA/cm^2 was observed while an increase in FF to 53.3% is observed. Further increasing the

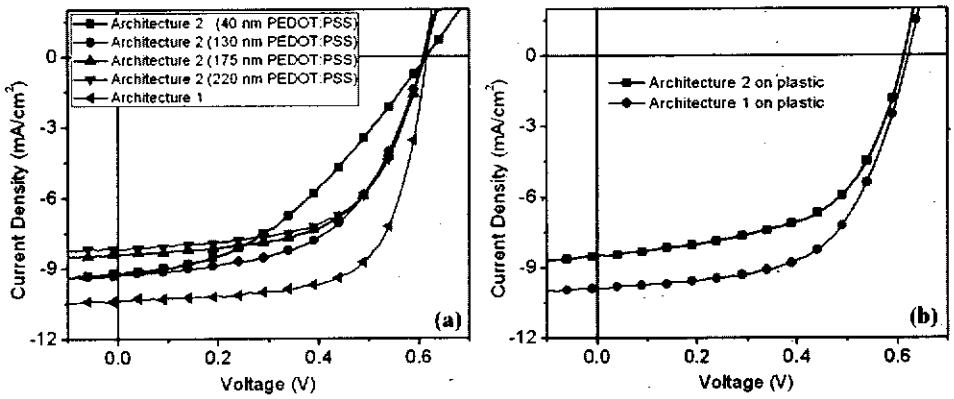

Figure 28. (a) Illuminated *J-V* characteristics of inverted devices fabricated from various thicknesses of PEDOT:PSS −5% DMSO as cathode electrodes on glass as compared to ITO-based cathode electrodes. (b) Illuminated *J-V* characteristics of inverted devices fabricated from PEDOT:PSS −5% DMSO cathode electrodes on plastic substrates and ITO-based cathode electrodes on plastic substrates. Adapted with permission from.[69] Copyright 2009 Elsevier. (Figure available in color online)

Table 8

Average device performance of inverted ZnO NP/C_{60}-SAM/P3HT:PCBM bulk-heterojunction solar cells fabricated using glass/PEDOT:PSS, plastic/PEDOT:PSS, glass/ITO and plastic/ITO as the cathode electrode and vacuum deposited Ag as the anode electrode. Adapted with permission from.[69] Copyright 2009 Elsevier

Electode (cathode)	Electrode (anode)	Voc (V)	Jsc (mA/cm^2)	FF (%)	PCE (%)
ITO/glass	Ag	0.62	10.3	66.6	4.2
PEDOT:PSS (~40 nm)/glass	Ag	0.61	9.6	39.4	2.3
PEDOT:PSS (~130 nm)/glass	Ag	0.61	9.4	53.3	3.1
PEDOT:PSS (~175 nm)/glass	Ag	0.61	8.6	57.2	3.0
PEDOT:PSS (~220 nm)/glass	Ag	0.61	8.2	60.0	3.0
ITO/plastic	Ag	0.61	9.9	61.2	3.7
PEDOT:PSS (~175 nm)/glass	Ag	0.62	8.4	57.7	3.0

thickness of the PEDOT:PSS films lead to a saturation in PCE to ~3.0%. Interestingly, the thicker PEDOT:PSS electrodes lead to higher FF, but a reduction in device J_{sc}. This trend can be correlated to the lower transparency and reduced sheet resistance with increasing layer thickness. The transparency and sheet resistance of the electrodes are an important consideration for the development of semi-transparent electrode materials in solar cells as they can affect both the photocurrent and fill factor. Lower transparency leads to a reduction of the potential photons that can be absorbed by the active layer therefore leads to lower photocurrent densities. Lower sheet resistance minimizes the resistive losses in the solar cells and improves fill factor. The charges lost from the lateral charge collection through the PEDOT:PSS electrode become much more apparent with higher sheet resistance. A dramatic improvement in the fill factor from 39.4% (~40 nm PEDOT:PSS) to 60.0% (~220 nm PEDOT:PSS) is observed by changing the sheet resistance from 2800 Ω/□ to 160 Ω/□. ITO/glass based solar cells had an average J_{sc} = 10.3 mA/cm^2, FF = 66.6%, and PCE of ~4.2%. The higher efficiency of the ITO substrates is due to the higher transparency (~10% higher) and lower sheet resistance (~10 times less) when compared to the ~220 nm thick PEDOT:PSS electrode.

Devices using PEDOT:PSS as the electrode in flexible substrates show similar performance (PCE ~3%) to that of solar cells fabricated onto glass substrates (Fig. 28(b)). The PCE is still lower in efficiency compared to ITO based plastic substrates which have an average PCE of ~3.7%. An important consideration for the development of organic solar cells that is often ignored is the mechanical device stability. Flexible solar cell devices using ITO and PEDOT:PSS electrodes were subjected to a cyclic bending (bend radius ~7.4 mm) test to evaluate the mechanical stability. Figure 29(a) shows the *J-V* characteristics of a flexible ITO based electrode device subjected to multiple bending cycles. A decrease in J_{sc} and FF is observed with devices using an ITO electrode and after 300 bending cycles showed only a ~50% PCE retention. Devices fabricated from the PEDOT:PSS electrodes show negligible degradation in J_{sc} and V_{oc}, but some slight degradation in FF after multiple bend cycles (Fig. 29(b)). In contrast to the ITO devices, the PEDOT:PSS electrodes retained ~92% of its original PCE even after 300 bending cycles (Fig 29(c)). Improving the mechanical stability will become important for commercial realization of low-cost polymer solar cells.

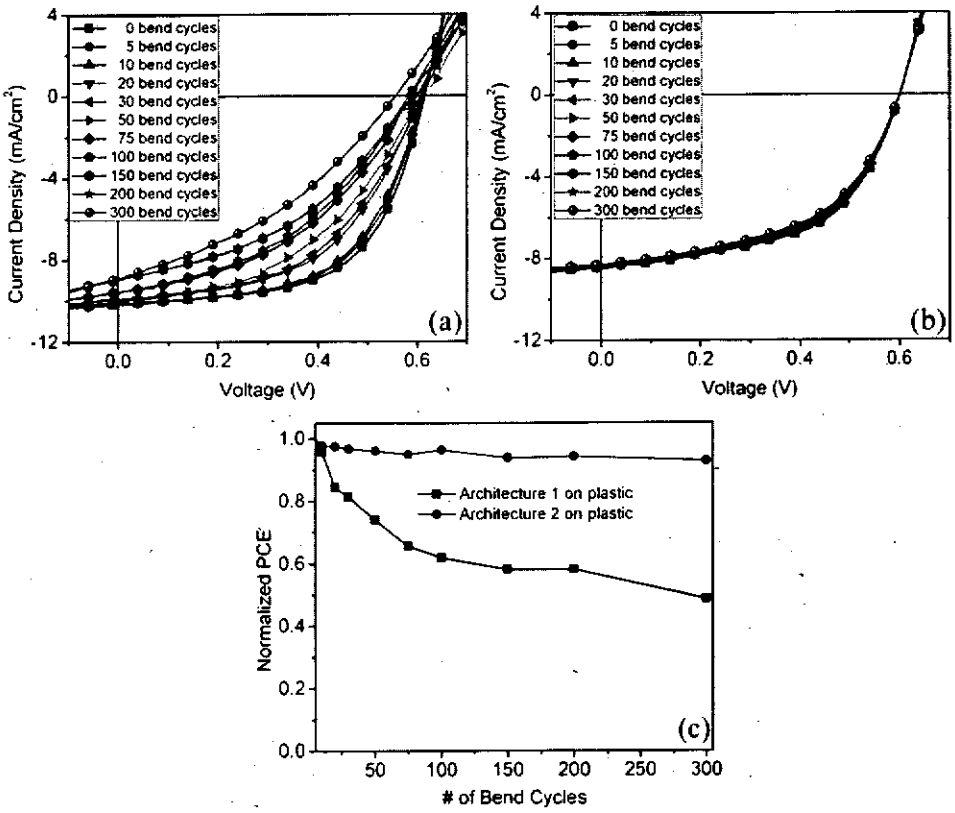

Figure 29. Plot of illuminated *J-V* characteristics of inverted devices fabricated from flexible ITO electrode substrates under multiple bending cycles. (b) Plot of illuminated *J-V* characteristics of inverted devices fabricated from flexible PEDOT:PSS −5% DMSO electrode substrates under multiple bending cycles. (c) Comparison of the normalized power conversion efficiency of devices fabricated from flexible ITO and flexible PEDOT:PSS electrodes as a function of bending cycles. Adapted with permission from.[69] Copyright 2009 Elsevier. (Figure available in color online)

3. Conclusions

In conclusion, the inverted device architecture is a promising architecture for the development of the more ideal polymer-based solar cell when compared to the conventional device architecture. This architecture allows for solution processing techniques to deposit the various layers onto flexible substrates allowing them to be potentially processed by industrial roll-to-roll type fabrication. In addition, the inverted device architecture is more stable to ambient due the use of higher work function metals as the top electrode. These higher work function electrodes also allow for the potential for coating the top metal electrode by a printing and coating processes that will help to minimize fabrication costs. An integrated engineering approach to develop materials, devices and improve interfaces and processing to improve the performance of inverted solar cell is described. Amorphous fullerenes were processed into the BHJ active layer of inverted solar cells showing improved thermal and morphological stability compared to devices processed with PCBM. The interfaces of the metal oxides (ZnO, TiO_2) in the inverted architecture were improved by using self-assembled monolayers which help to improve the charge transfer properties at the interface

and help to improve the bulk-heterojunction morphology leading to high efficiency solar cells. Solution processed electrodes to replace vacuum deposited metal electrodes and expensive ITO electrodes in inverted solar cells are demonstrated showing the feasibility for developing roll-to-roll type processing of solar cells. More research in the development of the inverted solar cell device architecture to further improve the efficiency and roll-to-roll type processibility is necessary in order for polymer-based solar cell to be fabricated in large-scale production.

Acknowledgements

The authors appreciate the financial support through the National Science Foundation STC program under DMR-0120967, the DOE "Future Generation Photovoltaic Devices and Process" program under DE-FC36-08GO18024/A000, the Office of Naval Research program under N00014-08-1-1129, the AFOSR "Interface Engineering" program under FA9550-09-1-0426, and the World Class University (WCU) program through the National Research Foundation of Korea under the Ministry of Education, Science and Technology (R31-10035). A. K. Y. Jen thanks the Boeing-Johnson Foundation for financial support.

References

1. Brabec, C. J.; Sariciftci, N. S.; Hummelen, J. C. "Plastic solar cells," *Adv. Funct. Mater.*, **2001**, *11*(15), 15–26.
2. Ma, W. L.; Yang, C. Y.; Gong, X.; Lee, K.; Heeger, A. J. "Thermally stable, efficient polymer solar cells with nanoscale control of the interpenetrating network morphology," *Adv. Funct. Mater.*, **2005**, *15*, 1617–1622.
3. Li, G.; Shrotyriya, V.; Huang, J. S.; Yao, Y.; Moriarty, T.; Emery, K.; Yang, Y. "High-efficiency solution processable polymer photovoltaic cells by self-organization of polymer blends," *Nature Mater.*, **2005**, *4*, 864–868.
4. Peet, J.; Kim, J. Y.; Coates, N. E.; Ma, W.; Moses, D.; Heeger, A. J.; Bazan, G. C. "Efficiency enhancement in low-bandgap polymer solar cells by processing with alkane dithiols," *Nature. Mater.*, **2007**, *6*, 497–500.
5. Liang, Y. Y.; Wu, Y.; Feng, D.; Tsai, S.-T.; Son, H.-J.; Li, G.; Yu, L. "Development of new semiconducting polymers for high performance solar cells," *J. Am. Chem. Soc.*, **2009**, *131*(1), 56–57.
6. Liang, Y. Y.; Feng, D.; Wu, Y.; Tsai, S.-T.; Li, G.; Ray, C.; Yu, L. "Highly efficient solar cell polymers developed via fine-tuning of structural and electronic properties," *J. Am. Chem. Soc.*, **2009**, *131*(22), 7792–7799.
7. Wong, K. W.; Yip, H. L.; Luo, Y.; Wong, K. Y.; Lau, W. M.; Low, K. H.; Chow, H. F.; Gao, Z. Q.; Yeung, W. L.; Chang, C. C. "Blocking reactions between indium-tin oxide and poly(3,4–3thylenedioxythiophene):poly(styrene sulphonate) with a self-assembly monolayer," *Appl. Phys. Lett.*, **2002**, *80*, 2788–2790.
8. de Jong, M. P.; van IJzendoorn, L. J.; de Voigt, M. J. A. "Stability of the interface between indium-tin oxide and poly(3,4-ethylenedioxythiophene)/poly(styrenesulphonate) in polymer light-emitting diodes," *Appl. Phys. Lett.*, **2000**, *77*, 2255–2257.
9. Hains, A. W.; Marks, T. J. "High-efficiency hole extraction/electron-blocking layer to replace poly(3,4–3thylenedioxythiophene):poly(styrene sulphonate) in bulk-heterojunction polymer solar cells," *Appl. Phys. Lett.*, **2008**, *92*, 023504–023506.
10. Hau, S. K.; Yip, H. L.; Baek, N. S.; Zou, J.; O'Malley, K.; Jen, A. K. Y. "Air-stable inverted flexible polymer solar cells using zinc oxide nanoparticles as an electron selective layer," *Appl. Phys. Lett.*, **2008**, *92*, 253301–253303.

11. Lee, K.; Kim, J. Y.; Park, S. H.; Kim, S. H.; Cho, S.; Heeger, A. J. "Air-stable polymer electronic devices," *Adv. Mater.*, **2007**, *19*, 2445–2249.
12. Kim, J. Y.; Kim, S. H.; Lee, H. H.; Lee, K.; Ma, W.; Gong, X.; Heeger, A. J. "New architecture for high-efficiency polymer photovoltaic cells using solution-based titanium oxide as an optical spacer," *Adv. Mater.*, **2006**, *18*, 572–576.
13. Yip, H.-L.; Hau, S. K.; Baek, N. S.; Ma, H.; Jen, A. K.-Y. "Polymer solar cells that use self-assembled monolayer modified ZnO/Metals as cathodes," *Adv. Mater.*, **2008**, *20*, 2376–2382.
14. Hau, S. K.; Yip, H.-L.; Leong, K.; Jen, A. K.-Y. "Spraycoating of silver nanoparticle electrodes for inverted polymer solar cells," *Org. Electron.*, **2009**, *10*, 719–723.
15. Girotto, C.; Rand, B. P.; Steudel, S.; Genoe, J.; Heremans, P. "Nanoparticle-based spray-coated silver top contacts for efficient polymer solar cells," *Org. Electron.*, **2009**, *10*, 735–740.
16. Krebs, F. C. "Air stable polymer photovoltaics based on process free from vacuum steps and fullerenes," *Solar Energy Mater. and Solar Cells.*, **2008**, *92*, 715–726.
17. Glatthaar, M.; Niggemann, M.; Zimmermann, B.; Lewer, P.; Riede, M.; Hinsch, A.; Luther, J. "Organic solar cells using inverted layer sequence," *Thin Solid Films.*, **2005**, *491*, 298–300.
18. Chen, F. C.; Wu, J. L.; Lee, C. L.; Huang, W. C.; Chen, H. M. P.; Chen, W. C. "Flexible polymer photovoltaic devices prepared with inverted structures on metal foils," *IEEE Electron. Device Lett.*, **2009**, *30*, 727–729.
19. Hsiao, Y. S.; Chen, C. P.; Chao, C. H.; Whang, W. T. "All-solution-processed inverted polymer solar cells on granular surface-nickelized polyimide," *Org. Electron.*, **2009**, *10*, 551–561.
20. Li, G.; Chu, C. W.; Shrotriya, V.; Huang, J.; Yang, Y. "Efficient inverted polymer solar cells," *Appl. Phys. Lett.*, **2006**, *88*, 253503–253505.
21. Liao, H. H.; Chen, L. M.; Xu, Z.; Li, G.; Yang, Y. "Highly efficient inverted polymer solar cell by low temperature annealing of Cs_2CO_3 interlayer," *Appl. Phys. Lett.*, **2008**, *92*, 173303–173305.
22. Zhao, D. W.; Liu, P.; Sun, X. W.; Tan, S. T.; Ke, L.; Kyaw, A. K. K. "An inverted organic solar cell with an ultrathin Ca electron-transporting layer and MoO_3 hole-transporting layer," *Appl. Phys. Lett.*, **2009**, *95*, 153304–153306.
23. White, M. S.; Olson, D. C.; Shaheen, S. E.; Kopidakis, N.; Ginley, D. S. "Inverted bulk-heterojunction organic photovoltaic device using solution-derived ZnO underlayer," *Appl. Phys. Lett.*, **2006**, *87*, 143517–143519.
24. Hau, S. K.; Yip, H. L.; Ma, H.; Jen, A. K. Y. "High performance ambient processed inverted polymer solar cells through interfacial modification with a fullerene self-assembled monolayer," *Appl. Phys. Lett.*, **2008**, *93*, 233304–233306.
25. Waldauf, C.; Morana, M.; Denk, P.; Schilinsky, P.; Coakley, K.; Choulis, S. A.; Brabec, C. J. "Highly efficient inverted organic photovoltaics using solution based titanium oxide as electron selective contact," *Appl. Phys. Lett.*, **2006**, *89*, 233517–233519.
26. Steim, R.; Choulis, S. A.; Schilinsky, P.; Brabec, C. J. "Interface modification for highly efficient organic photovoltaics," *Appl. Phys. Lett.*, **2008**, *92*, 093303–093306.
27. Hau, S. K.; Yip, H. L.; Acton, O.; Baek, N. S.; Ma, H.; Jen, A. K. Y. "Interfacial modification to improve inverted polymer solar cells," *J. Mater. Chem.*, **2008**, *18*, 5113–5119.
28. Kyaw, A. K. K.; Sun, X. W.; Jiang, C. Y.; Lo, G. Q.; Zhao, D. W.; Kwong, D. L. "An inverted organic solar cell employing a sol-gel derived ZnO electron selective layer and thermal evaporated MoO_3 hole selective layer," *Appl. Phys. Lett.*, **2008**, *93*, 221107–221109.
29. Tao, C.; Ruan, S. P.; Zhang, X. D.; Xie, G. H.; Shen, L.; Kong, X. Z.; Dong, W.; Liu, C. X.; Chen, W. Y. "Performance improvement of inverted polymer solar cells with different top electrodes by introducing a MoO_3 buffer layer," *Appl. Phys. Lett.*, **2008**, *93*, 193307–193309.
30. Schmidt, H.; Flugge, H.; Winkler, T.; Bulow, T.; Riedl, T.; Kowalsky, W. "Efficient semitransparent inverted organic solar cells with indium tin oxide top electrode," *Appl. Phys. Lett.*, **2009**, *94*, 243302–243304.
31. Tao, C.; Ruan, S. P.; Xie, G. H.; Kong, X. Z.; Shen, L.; Meng, F. X.; Liu, C. X.; Zhang, X. D.; Dong, W.; Chen, W. Y. "Role of tungsten oxide in inverted polymer solar cells," *Appl. Phys. Lett.*, **2009**, *94*, 043311–043313.

32. Chan, M. Y.; Lee, C. S.; Lai, S. L.; Fund, M. K.; Wong, F. L.; Sun, H. Y.; Lau, K. M. Lau; Lee, S. T. "Efficient organic photovoltaic devices using a combination of exciton blocking layer and anodic buffer layer," *J. Appl. Phys.*, **2006**, *100*, 094506–094509.
33. Huang, J. S.; Chou, C. Y.; Liu, M. Y.; Tsai, K. H.; Lin, W. H.; Lin, C. F. "Solution-processed vanadium oxide as an anode interlayer for inverted polymer solar cells hybridized with ZnO nanorods," *Org. Electron.*, **2009**, *10*, 1060–1065.
34. Chu, C. W.; Chen, C. W.; Li, S. H.; Wu, E. H. E.; Yang, Y. "Integration of organic light-emitting diode and organic transistor via a tandem structure," *Appl. Phys. Lett.*, **2005**, *86*, 253503–253505.
35. Kido, J.; Matsumoto, T.; Nakada, T.; Endo, J.; Mori, K.; Kawamura, N. Kawamura; Yokoi, A., *SID 03 Digest.*, **2003**, *984*, 984–979.
36. Li, C. Y.; Wen, T. C.; Guo, T. F. "Sulfonated poly(diphenylamine) as a novel hole-collecting layer in polymer photovoltaic cells," *J. Mater. Chem.*, **2008**, *18*, 4478–4482.
37. van Bavel, S.; Sourty, E.; de With, G.; Frolic, K.; Loos, J. "Relation between photoactive layer thickness, 3D morphology, and device performance in P3HT/PCBM bulk-heterojunction solar cells," *Macromolecules.*, **2009**, *42*, 7396–7403.
38. Kumar, A.; Li, G.; Hong, Z. R.; Yang, Y. "High efficiency polymer solar cells with vertically modulated nanoscale morphology," *Nanotechnology.*, **2009**, *20*, 165202–165205.
39. Campoy-Quiles, M.; Ferenczi, T.; Agostinelli, T.; Etchegoin, P. G.; Kim, Y.; Anthopoulos, T. D.; Stavrinou, P. N.; Bradley, D. D. C. Bradley; Nelson, J. "Morphology evolution via self-organization and lateral, and vertical diffusion in polymer: fullerene solar cell blends," *Nature Mater.*, **2008**, *7*, 158–164.
40. Xu, Z.; Chen, L. M.; Yang, G. W.; Huang, C. H.; Hou, J. H.; Wu, Y.; Li, G.; Hsu, C. S.; Yang, Y. "Vertical phase separation in poly(3-hexylthiophene):fullerene derivative blends and its advantage for inverted structure solar cells," *Adv. Funct. Mater.*, **2009**, *19*, 1227–1234.
41. Germack, D. S.; Chan, C. K.; Hamadani, B. H.; Richter, L. J.; Fischer, D. A.; Gundlach, D. J.; DeLongchamp, D. M. "Substrate-dependent interface composition and charge transport in films for organic photovoltaics," *Appl. Phys. Lett.*, **2009**, *94*, 233303–233305.
42. Lloyd, M. T.; Olson, D. C.; Lu, P.; Fang, E.; Moore, D. L.; White, M. S.; Reese, M. O.; Ginley, D. S.; Hsu, J. W. P. "Impact of contact evolution on the shelf life of organic solar cells," *J. Mater. Chem.*, **2009**, *19*, 7638–7642.
43. Kim, J. B.; Kim, C. S.; Kim, Y. S.; Loo, Y. L. "Oxidation of silver electrodes induces transition from conventional to inverted photovoltaic characteristics in polymer solar cells," *Appl. Phys. Lett.*, **2009**, *95*, 183301–183303.
44. Swinnen, A.; Haeldermans, I.; vande Ven, M.; D'Haen, J.; Vanhoyland, G.; Aresu, S.; D'Olieslaeger, M. D.; Manca, J. "Tuning the dimensions of C_{60}-based needlelike crystals in blended thin films," *Adv. Funct. Mater.*, **2005**, *16*, 760–765.
45. Muller, C.; Ferenczi, T. A. M.; Campoy-Quiles, M.; Frost, J. M.; Bradley, D. D. C.; Smith, P.; Stingelin-Stutzmann, N.; Nelson, J. "Binary organic photovoltaic blends: a simple rationale for optimum compositions," *Adv. Mater.*, **2008**, *20*, 3510–3515.
46. Woo, C. H.; Thompson, B. C.; Kim, B. J.; Toney, M. F.; Frechet, J. M. "The influence of poly(3-hexylthiophene) regioregularity on fullerene-composite solar cell performance," *J. Am. Chem. Soc.*, **2008**, *130*, 16324–16329.
47. Sivula, K.; Luscombe, C. K.; Thompson, B. C.; Frechet, J. M. "Enhancing the thermal stability of polythiophene:fullerene solar cells by decreasing effective polymer regioregularity," *J. Am. Chem. Soc.*, **2006**, *128*, 13988–13989.
48. Sivula, K.; Ball, Z. T.; Watanabe, N.; Frechet, J. M. "Amphiphilic diblock copolymer compatibilizers and their effect on the morphology and performance of polythiophene:fullerene solar cells," *Adv. Mater.*, **2006**, *18*, 206–210.
49. Zhou, Z. Y.; Chen, X. W.; Holdcroft, S. "Stabilizing bicontinuous nanophase segregation in pi CP-C_{60} donor-acceptor blends," *J. Am. Chem. Soc.*, **2008**, *130*, 11711–11718.
50. Zhang, Y.; Yip, H. L.; Acton, O.; Hau, S. K.; Huang, F.; Jen, A. K.-Y. "A simple and effective way of achieving highly efficient and thermally stable bulk-heterojunction polymer solar cells using amorphous fullerene derivatives as electron acceptor," *Chem. Mater.*, **2009**, *21*, 2598–2600.

51. Hummelen, J. C.; Knight, B. W.; LePeq, F.; Wudl, F.; Yao, J.; Wilkins, C. L. "Preparation and characterization of fulleroid and methanofullerene derivatives," *J. Org. Chem.*, **1995**, *60*, 532–538.
52. Zheng, L. P.; Zhou, Q. M.; Deng, X. Y.; Yuan, M.; Yu, G.; Cao, Y. "Methanofullerenes used as electron acceptors in polymer photovoltaic devices," *J. Phys. Chem. B.*, **2004**, *108*, 11921–11926.
53. Yang, C.; Kim, J. Y.; Cho, S.; Lee, J. K.; Heeger, A. J.; Wudl, F. "Functionalized methanofullerenes used as n-type materials in bulk-heterojunction polymer solar cells and in field-effect transistors," *J. Am. Chem. Soc.*, **2008**, *130*, 6444–6450.
54. Chua, L. L.; Zaumseil, J.; Chang, J.-F.; Ou, E. C.-W.; Ho, P. K.-H.; Sirringhaus, H.; Friend, R. H. "General observation of n-type field-effect behaviour in organic semiconductors," *Nature.*, **2005**, *434*, 194–199.
55. Khodabakhsh, S.; Sanderson, B. M.; Nelson, J.; Jones, T. S. "Using self-assembling dipole molecules to improve charge collection in molecular solar cells," *Adv. Func. Mater.*, **2006**, *16*, 95–100.
56. Armstrong, N. R.; Carter, C.; Donley, C.; Simmonds, A.; Lee, P.; Brumbach, M.; Kippelen, B.; Domercq, B.; Yoo, S. "Interface modification of ITO thin films: Organic photovoltaic cells," *Thin Solid Films.*, **2003**, *445*, 342–352.
57. Kim, J. S.; Park, J. H.; Lee, J. H.; Jo, J.; Kim, D. -Y.; Cho, K. "Control of the electrode work function and active layer morphology via surface modification of indium tin oxide for high efficiency organic photovoltaics," *Appl. Phys. Lett.*, **2007**, *91*, 112111–112113.
58. Goh, C.; Scully, S. R.; McGehee, M. D. "Effects of molecular interface modification in hybrid organic-inorganic photovoltaic cells," *J. Appl. Phys.*, **2007**, *101*, 114503–114514.
59. Moser, J.; Punchihewa, S.; Infelta, P. P.; Gratzel, M. "Surface complexation of colloidal semiconductors strongly enhances interfacial electron-transfer rates," *Langmuir.*, **1991**, *7*, 3012–3018.
60. Sariciftci, N. S.; Smilowitz, L.; Heeger, A. J.; Wudl, F. "Photoinduced electron-transfer from a conducting polymer to buckminsterfullerene," *Science.*, **1992**, *258*, 1474–1476.
61. Kim, D. H.; Jang, Y.; Park, Y. D.; Cho, K. "Surface-induced conformational changes in poly(3-hexylthiophene) monolayer films," *Langmuir.*, **2005**, *21*, 3203–3206.
62. Morana, M.; Koers, P.; Waldauf, C.; Koppe, M.; Muehlbacher, D.; Denk, P.; Scharber, M.; Waller, D.; Brabec, C. "Organic field-effect devices as tool to characterize the bipolar transport in polymer-fullerene blends: the case of P3HT:PCBM," *Adv. Funct. Mater.*, **2007**, *17*, 3274–3283.
63. Kim, Y.; Choulis, S. A.; Nelson, J.; Bradley, D. D. C.; Cook, S.; Durrant, J. R. "Device annealing effect in organic solar cells with blends of regioregular poly(3-hexylthiophene) and soluble fullerene," *Appl. Phys. Lett.*, **2005**, *86*, 063502–063504.
64. Beek, W. J. E.; Wienk, M. M.; Kemerink, M.; Yang, X.; Janssen, R. A. J. "Hybrid zinc oxide conjugated polymer bulk heterojunction solar cells," *J. Phys. Chem. B.* **2005**, *109*, 9505–9516.
65. Hau, S. K.; O'Malley, K. M.; Cheng, Y. J.; Yip, H. L.; Ma, H.; Jen, A. K.-Y. "Optimization of active layer and anode electrode for high-performance inverted bulk-heterojunction solar cells," *IEEE J. Selected Topics in Quantum Electronics.*, **2010**, *99* (in press).
66. Mihailetchi, V. D.; Blom, P. W. M.; Hummelen, J. C.; Rispens, M. T. "Cathode dependence of the open-circuit voltage of polymer:fullerene bulk heterojunction solar cells," *J. Appl. Phys.*, **2003**, *94*, 6849–6854.
67. Reese, M. O.; White, M. S.; Rumbles, G.; Ginley, D. S.; Shaheen, S. E. "Optimal negative electrodes for poly(3-hexyltiophene):[6,6]-phenyl C_{61}-butyric methyl ester bulk heterojunction photovoltaic devices," *Appl. Phys. Lett.*, **2008**, *92*, 053307–053309.
68. Jönsson, S. K. M.; Salaneck, W. R.; Fahlman, M. "X-ray photoelectron spectroscopy study of the metal/polymer contacts involving aluminum and poly(3,4-ethylenedioxythiophene)-poly(styrenesulfonic acid) derivatives," *J. Mater. Res.*, **2003**, *18*, 1219–1226.
69. Hau, S. K.; Yip, H. L.; Zou, J.; Jen, A. K.-Y. "Indium tin oxide-free semi-transparent inverted polymer solar cells using conducting polymer as both bottom and top electrodes," *Org. Electron.*, **2009**, *10*, 1401–1407.